NASA CONTRACTOR
REPORT

NASA CR-120482

(NASA-CR-120482) CONVECTION EFFECTS ON
SKYLAB EXPERIMENTS M551, M552, AND M553,
PHASE C REPORT (Lockheed Missiles and
Space Co.) 96 p HC $4.75 CSCL 22C

N75-10120

Unclas
G3/12 52719

CONVECTION EFFECTS ON SKYLAB EXPERIMENTS M551, M552, and M553

Phase C Report

By S. V. Bourgeois
Lockheed Missiles and Space Company, Inc.
Huntsville Research and Engineering Center
Huntsville, Alabama

Prepared for

NASA-GEORGE C. MARSHALL SPACE FLIGHT CENTER
Marshall Space Flight Center, Alabama 35812

TECHNICAL REPORT STANDARD TITLE PAGE

1. REPORT NO.
NASA CR-120482

2. GOVERNMENT ACCESSION NO.

3. RECIPIENT'S CATALOG NO.

4. TITLE AND SUBTITLE
Convection Effects On Skylab Experiments M551, M552 and M553
Phase C Report

5. REPORT DATE
December 1973

6. PERFORMING ORGANIZATION CODE

7. AUTHOR(S)
S. V. Bourgeois

8. PERFORMING ORGANIZATION REPORT #

9. PERFORMING ORGANIZATION NAME AND ADDRESS
Lockheed Missiles and Space Company, Inc.
Huntsville Research and Engineering Center
Huntsville, Alabama

10. WORK UNIT NO.

11. CONTRACT OR GRANT NO.

12. SPONSORING AGENCY NAME AND ADDRESS
National Aeronautics and Space Administration
Washington, D. C. 20546

13. TYPE OF REPORT & PERIOD COVERED
Contractor Report

14. SPONSORING AGENCY CODE

15. SUPPLEMENTARY NOTES

16. ABSTRACT

This report describes an analysis of Skylab Experiments M551 (Metals Melting), M552 (Exothermic Brazing), and M553 (Sphere Forming). The primary objective is the study of convection in the molten metals and their attendant solidification theory. Particular attention is given to clarifying the effects of reduced gravity on molten metal flow and solidification. Based on an analysis of physical forces and solidification theory expected for ground-based and Skylab processing, low-g variations were predicted for each experiment. A comparison was then made with the Skylab results available to date. Both metallurgical analyses of other investigators and movies of ground-based and Skylab samples were utilized. Several low-g variations in Skylab processed materials were successfully predicted based on expected variations in physical forces and fluid convection. The same analysis also successfully predicted several features in the Skylab-processed materials which were identical to terrestrially-processed materials. These results are summarized in the conclusion section for each experiment.

17. KEY WORDS

18. DISTRIBUTION STATEMENT
Unclassified - Unlimited
W K Vardaman

19. SECURITY CLASSIF. (of this report)
Unclassified

20. SECURITY CLASSIF. (of this page)
Unclassified

21. NO. OF PAGES
97

22. PRICE
NTIS

MSFC - Form 3292 (Rev December 1972)

For sale by National Technical Information Service, Springfield, Virginia 22151

FOREWORD

This report summarizes the results of the Phase C portion of Contract NAS8-27015 for the 5-month period ending 1 July 1973. This effort was performed by the Lockheed-Huntsville Research & Engineering Center for NASA-Marshall Space Flight Center.

The NASA Contracting Officer's Representative (COR) for this study is Mr. T. C. Bannister, S&E-SSL-T. The NASA principal investigators for this study are Mr. R. M. Poorman (M551), S&E-ASTN-MM; Mr. J. R. Williams (M552), S&E-PT-M; and Mr. E. A. Hasemeyer (M553), S&E-PT-MWM.

TABLE OF CONTENTS

PRECEDING PAGE BLANK NOT FILMED

CONTENTS (Continued)

LIST OF ILLUSTRATIONS

LIST OF TABLES

NOMENCLATURE

A	Area
B	Magnetic Induction
C	Heat Capacity
c	Concentration, Mass or Moles per Unit Volume
D	Diameter, Diffusivity, Displacement Current
d	Differential Operator
E	Electric Field Intensity
e	Base of Natural Logarithms
F	Force
f	Force Component
G	Temperature Gradient of the Melt at Solidification Front
g	Acceleration of Gravity
g_E	Sea Level Gravity on Earth, 9.8 m/sec^2
H	Magnetic Field Intensity
h	Individual Coefficient of Heat Transfer
I	Electron Current
J	Electrical Current Density
K	Coefficient of Isothermal Volumetric Compressibility, $\frac{1}{\rho}\left(\frac{\partial \rho}{\partial P}\right)_T$
k	Mass Transfer Coefficient, Thermal Conductivity
L	Length
M_w	Molecular Weight
m	Slope of Equilibrium Curve

NOMENCLATURE (Continued)

$\dot{m}$	Mass Flux Due to Evaporation
N_i	Mole Fraction of Component i
$\vec{n}$	Unit Normal Vector
n_i	Moles of Component i
P	Pressure, Power, Temperature Rate ($^{\circ}$K/sec)
P_V	Vapor Pressure
p	Partial Pressure
$\dot{Q}$	Rate of Internal Heat Generation
q	Heat
$\dot{q}$	Rate of Heat Flow
R	Universal Gas Constant, Resistance, Outer Radius, Crystal Interface Growth Rate
r	Radius
S	Surface Tension Gradient with Temperature
T	Temperature
T_M	Melting Point
ΔT	Degree of Undercooling
t	Time
U	Internal Energy
u	Longitudinal Component of Local Velocity, Velocity in General
V	Volume
$\vec{V}$	Velocity Vector
v	Lateral Component of Local Velocity, Nominal Velocity

NOMENCLATURE (Continued)

w	Normal Component of Local Velocity
x	Longitudinal Distance from Datum Plane
y	Lateral Distance from Datum Plane
z	Vertical Distance from Datum Plane

GREEK LETTERS

α	Thermal Diffusivity
β	Coefficient of Isobaric Volumetric Thermal Expansion, $-\frac{1}{\rho}\left(\frac{\partial \rho}{\partial T}\right)_P$
γ	Ratio of Specific Heats, Ratio of Buoyancy over Surface Tension Force
∇	Grad or del Operator
∂	Partial Differential Operator
δ	Position of Melt/Crystal Interface, Boundary Layer Width, Variation Operator
Δ	Difference, Finite Difference Operator
ϵ	Emissivity (Radiation)
ϵ'	Permittivity (Dielectric Constant)
η	Efficiency
θ	Contact Angle
λ	Latent Heat of Phase Change, Wave Length, Interlammellar Eutectic Spacing
λ_f	Latent Heat of Fusion
λ_s	Latent Heat of Sublimation

NOMENCLATURE (Continued)

λ_v	Latent Heat of Vaporization
μ	Viscosity
μ'	Magnetic Permeability
ν	Kinematic Viscosity
ρ	Density, Electrical Resistivity
ρ_e	Electrical Charge Density
σ	Surface Tension, Stefan-Boltzmann Constant
σ_{LV}	Surface Energy at Liquid-Vapor Interface
σ_{LS}	Surface Energy at Liquid-Solid Interface
σ_{SV}	Surface Energy at Solid-Vapor Interface
σ'	Electrical Conductivity
ϕ	Angle
Φ	Viscous Dissipation
ω	Frequency, Angular Velocity

DIMENSIONLESS NUMBERS

Bo	Bond Number, $\rho g L^2/\sigma$ or $\rho g L^2/ST$
N_{MI}	Magnetic Interaction Number, $B^2L/2\mu' ST$
Ma	Marangoni Number, $S\Delta TL/\rho\nu\alpha$
Ma_c	Critical Marangoni Number
Nu	Nusselt Number, hL/k
Oh	Ohnesorge Number, $\mu/\sqrt{\rho LST}$
Pr	Prandtl Number, $\mu C/k$

NOMENCLATURE (Continued)

Ra	Rayleigh Number, $g\beta\Delta T L^3/\nu\alpha$
Ra_c	Critical Rayleigh Number
St	Stokes Number, $\mu t/\rho L$
Sf	Stefan Number, $\sigma T^3 L/k$
We	Weber Number, $\rho v^2 L/\sigma$

SUBSCRIPTS

c	Critical
f	Fraction
G	Vapor
i	Generalized Component, Interface
j	Generalized Component
L	Liquid, Liquidus
M	Melting Point
m	Mean
o	Initial
P	Constant Pressure
S	Solidus, Solid
s	Surface
T	Constant Temperature, Total
t	Tangential, Terminal
V	Constant Volume, Vapor Phase
W	Wall

NOMENCLATURE (Continued)

SUPERSCRIPTS

→	Denotes Vector Quantity
·	First Derivative with Time
··	Second Derivative with Time

SECTION I. INTRODUCTION

Skylab Experiments M551 (Metals Melting), M552 (Exothermic Brazing), M553 (Sphere Forming), and M566 (Aℓ-Cu Eutectic Growth) were analyzed under Contract NAS8-27015. Their primary objective is the study of convection in the molten metals and their attendant solidification theory. Particular attention is given to clarifying the effects of reduced gravity on molten metal flow and solidification.

Under Phase A of this contract, a ground-based study plan was prepared. A summary report [1] was issued on this 10-week phase ending July 1972. The ground study program defined in Phase A was performed in Phase B which ended July 1973 and a summary report was issued [2]. The phase C portion of this contract is the subject of the present report and consists of a comparative analysis between Skylab I flight specimens and data versus those ground-based and KC-135 specimens and data already processed. The Phase C segment will continue through January 1974. The reporting of Phase B and Phase C results for the M566 experiments will each be delayed approximately three months because this experiment will be flown on Skylab IV.

This Phase C report is concerned specifically with the Metals Melting Experiment, the Exothermic Brazing Experiment, and the Sphere Forming Experiment performed in the M512 facility during the Skylab I mission of May-June 1973. These experiments are described briefly as follows:

<u>M551 Metals Melting Experiment:</u> Three sample disks, each containing three metal specimens of varying thicknesses, are to be rotated automatically at a controlled speed of 2.5 rpm under an electron beam gun such that an electron beam weld seam is produced in the metal specimen at a radius of 6 cm. Disk materials include 2219 aluminum, 321 stainless steel and tantalum. During the continuous weld portion of each disk, both full and partial penetration of the disk will be achieved by having a constant power input but a varying disk thickness. For each disk, the continuous weld will be followed by a dwell portion. In the dwell portion of the weld, the disk will remain stationary while the electron beam impinges on a thick segment of the disk, thus creating a large molten pool. The electron beam will then be shut off and the pool will be allowed to solidify.

<u>M552 Exothermic Brazing</u>: A technique for joining stainless steel tubes will be tested in this experiment and the flow and solidification behavior of weightless molten braze alloys will be studied. The joining technique will use a solid mixture that produces heat by exothermic chemical reaction to braze sleeves over 18.75-mm diameter

tubes, using a copper-silver-lithium braze alloy. A package containing four assemblies, each consisting of a tube with sleeve and performed braze alloy surrounded by exothermic material, will be mounted in the M512 facility's vacuum chamber. The exothermic reactions in the four assemblies will be ignited in sequence and the whole package will be returned to earth for analysis.

M553 Sphere Forming Experiment: Twenty-eight 6.35-mm diameter spherical specimens will be cast using the electron beam gun as a heat source. The specimens will be initially supported on two wheels by a sting. After melting is completed, the spheres will then be separated from their stings and allowed to solifify while free-flowing in the vacuum chamber. Specimens will consist of the following materials: pure nickel, Ni-1% Ag, Ni-30% Cu, and Ni-12% Sn.

The nominal operating conditions for the electron beam gun, braze units and the M512 vacuum chamber are given in Appendix A. This appendix also contains the updated convection sensitivity analysis for all the M512 experiments (M551, M552, M553 and M556) and a general discussion on the effects of convection and homogeneous nucleation on solidification.

For these particular Skylab experiments, the only significant difference between space and earth processing will be the lack of gravity. The maximum gravity level experienced during operation of the M551, M552 and M553 experiments aboard Skylab II was 7×10^{-4} g_E ($g_E = 9.8$ m/sec^2). Other environmental factors which may also differ from earth processing are the vacuum, radiation, electromagnetic and thermal conditions.

Gravity has no direct effect on grain structure or other properties of solidified material. These properties are determined by the crystallization kinetics which are controlled by short-range intermolecular forces; i.e., the temperature and concentration at the fluid-solid interface. Gravity has not been shown to have any significant direct effect on these forces, but can affect solidification indirectly through its direct effect on fluid motion. The three major indirect effects of gravity on solidification are:

- Sedimentation
- Bouyancy-Induced Convection, and
- Hydrostatic Pressure.

In addition to these three very important indirect effects, the lack of gravity will also afford the study of a more direct effect – the opportunity to obtain homogeneous nucleation. The long free-float times potentially available in space processing applications will allow melts to cool and nucleate without the deleterious effects of container walls. Wall effects are usually very strong in nucleation phenomena and prevent large degrees of supercooling from being attained in terrestrial processing. The remaining indirect effects are explained further below.

Sedimentation: This effect may be significant whenever heterogeneous mixtures exist in fluids, such as in monotectic, dispersed-particle, or fiber-reinforced composite casting. The denser of the immiscible materials will tend to settle unless colloidal or electrostatic attractions interfere. Also, in supercooled melts, segregation of freshly formed nuclei by gravity would affect the final grain structure. Nonmetallic inclusions, gas bubbles and voids, which usually exist in melts, are also distributed nonuniformly by gravity.

Convection: In terrestrial processing, gravity is the primary driving force for the convection of contained fluids when they are subjected to thermal or concentration gradients. Temperature gradients arise from external heating and cooling, whereas concentration gradients are usually produced internally (Soret effect and solute rejection at freezing interfaces which leads to "constitutional super-cooling"). These two gradients can produce density gradients large enough to induce buoyancy-driven flow. This fluid motion affects the temperature and concentration profiles within the fluid. This subsequently alters the shape and rate of movement of the freezing interface, because the kinetics of freezing depend on the local temperature and concentration. The degree of mixing caused by convection may be large enough to change the rate of solidification from kinetic to heat transfer or diffusion controlled which could drastically alter the grain structure. Examples of this convective effect on the transitions from planar to cellular or dendritic growth, from columnar to equiaxed eutectic structures, and from unidirectional to colonied or banded eutectic structures are cited frequently in the literature. Another effect of gravity-driven convection on solidification processes is that the bulk fluid movement, if rapid enough, can break delicate dendrite arms and thereby alter final grain structure. Furthermore, interlamellar spacing in eutectic growth and dendrite arm spacing are dependent on cooling rate which is a strong function of convection.

Hydrostatic Pressure: A body of fluid in a gravity field sustains a vertical pressure gradient as the bottom fluid must support the weight of the upper fluid. This pressure gradient distorts the shape of liquids on earth because the shape of a liquid surface is determined by the surface tension and the internal hydrostatic pressure (and adhesion if the liquid wets a solid surface). Distorted drops of liquid will result in nonsymmetrical solids upon freezing.

The following sections contain separate discussions for each experiment on the effects of microgravity on molten metal flow and solidification. For each experiment, the expected and actual low-g variations are discussed. In the M551 Metals Melting Experiment, the relative magnitudes of convection in the molten pool and their effect on grain structure and shape have been analyzed. In the M552 Exothermic Brazing Experiment, the effects of gravity on capillary flow and capillary "gap" limits have been studied. In the M553 Sphere Forming Experiment, the magnitude of convection has been determined and how the grain structure, shape and surface finish of the spherical specimens should be affected.

Visual observation of flight and ground specimens, films (M551 and M553), and reported observations of other M512 investigators' post-experiment metallurgical analyses have served as the basis for comparing flight test data and specimens in the Phase C study. These observations consisted of identifying convective stirring from film and identifying differences in structure, homogeneity, and/or unidirectionality in the post-experiment metallurgical analyses. Quantitative evaluations were limited because not all the results of other investigators have been reported to date.

SECTION II. M551 EXPERIMENT

The primary objective of this experiment is to study the melting and solidification of metals in reduced gravity. A second objective is to evaluate the electron beam (eb) process as a joining and cutting technique applicable to assembly and repair of structures in space. The primary goal of this particular study is to delineate the magnitude and pattern of the molten metal flow for both terrestrial and space flight processing conditions. From a knowledge of the convective differences and the other differences between terrestrial and space processing, the effects on grain structure and shape of the weld seam and dwell can be predicted. The "other" differences of space versus ground processing include differences in sedimentation and beading (lack of hydrostatic pressure in space) and possible differences in vibration, radiation and vacuum levels. These last three effects are not predictable to a precise degree of accuracy and are no doubt negligible in comparison to microgravity and therefore will not be considered important. Thus the following discussions compare the expected and actual low-g variations in the M551 experiment due to the convective differences between terrestrial and space processing.

A. RESULTS OF PREFLIGHT ANALYSES

A summary of the most significant preflight results is given below:

- The following physical forces are operative during the cutting, joining and dwell portions of this experiment:

  Gravity/Acceleration
  Surface Tension
  Lorentz (beam current)
  Electrostriction
  Magnetostriction
  Electrostatic Charges
  Solidification Shrinkage
  Thermal Expansion
  Vaporization
  eb Mechanical Pressure Force

- Significant molten metal motion should be exhibited in each of the specimens in both the dwell and weld (disk rotating) modes for both flight and ground tests.

- Both gravity and surface tension forces control molten metal flow in the dwell during M551 ground tests. These natural convection driving forces arise because of severe nonisothermality during heating.

- Surface tension will still provide an equal magnitude of convection for the dwell in zero-g, although the flow pattern may be different (see Appendix B).

- Spiking frequencies in the stainless steel partial penetration zones are dependent on gravity. The spiking phenomenon can be explained by oscillations of the melt caused by dynamic beam-melt interactions.

- The mechanical pressure force associated with the impinging electron beam will not cause unstable splattering in the dwell mode, even in absolute zero gravity. Thus, any splattering can be attributed to electromagnetic instabilities at the weld pool surface or to degassing.

- Sedimentation will not be a factor in this experiment, because vigorous stirring will occur both in terrestrial and Skylab operations.

The preceding conclusions were drawn from examination of color motion picture film taken during ground tests and from detailed examination of the descriptive differential equations which govern eb melting and solidification. The equations were examined using dimensional analysis [3 and 4] and the nominal operating and boundary conditions for this experiment and the M512 chamber (Appendix A). Detailed derivations and results are given in Appendix B.

It should also be mentioned that surface tension, gravity and the electromagnetic forces are the most significant of all the preceding physical forces for convective motion. On Earth, gravity and surface tension are equal and dominant; whereas, on Skylab, surface tension will be dominant, followed by electromagnetic, then by gravity. Furthermore, there are two primary effects of surface tension on melt behavior:

- The mean effect of uniform surface tension results in normal stresses at free surfaces which determine the shape of fluids.

- Nonuniform surface tension leads to tangential stresses at free surfaces which can induce fluid motion.

B. EXPECTED LOW-G VARIATIONS

Based on the preceding results and conclusions, the following predictions are made regarding the variations expected in the disk welds processed in the microgravity conditions aboard Skylab:

- Slightly different grain structure and/or dendrite arm spacing may result due to different melt flow patterns (see Appendix B).
- Lack of hydrostatic pressure and dominance of surface tension will allow dwell pool shape to be different (more spherical) and may cause shallower eb penetration.
- Spiking frequencies in the stainless steel partial penetration welds should be increased as much as 25 percent.

The different pool shape will occur because surface tension acts to pull the melt toward cooler surfaces which is away from the electron beam in this case. Assuming that the net gravitational field is always aligned with the beam in Skylab processing, the situations illustrated in Figure 1 will result regarding bulk melt behavior of the dwell pool. As seen in Figure 1a, surface tension dominance will pull the melt away from the beam, resulting in less resistance and deeper beam penetration than in terrestrial processing when heating from above. When heating from the side, however, terrestrial processing allows the melt to run out of the pool which will probably lead to even less resistance and more penetration than in space processing. Shallower dwell penetrations should be expected aboard Skylab because ground samples were processed as in Figure 1b.

C. ACTUAL LOW-G RESULTS

Specific evaluations which were to be performed for this experiment in the Phase C portion of the study include:

- Flight film examination and comparison with ground test films to investigate differences in magnitude (velocity) of convection and flow patterns.
- Microstructure and grain size (to be obtained from other investigators) examination and comparison with ground test results to observe if different melt shapes and convection patterns had any significant effects.

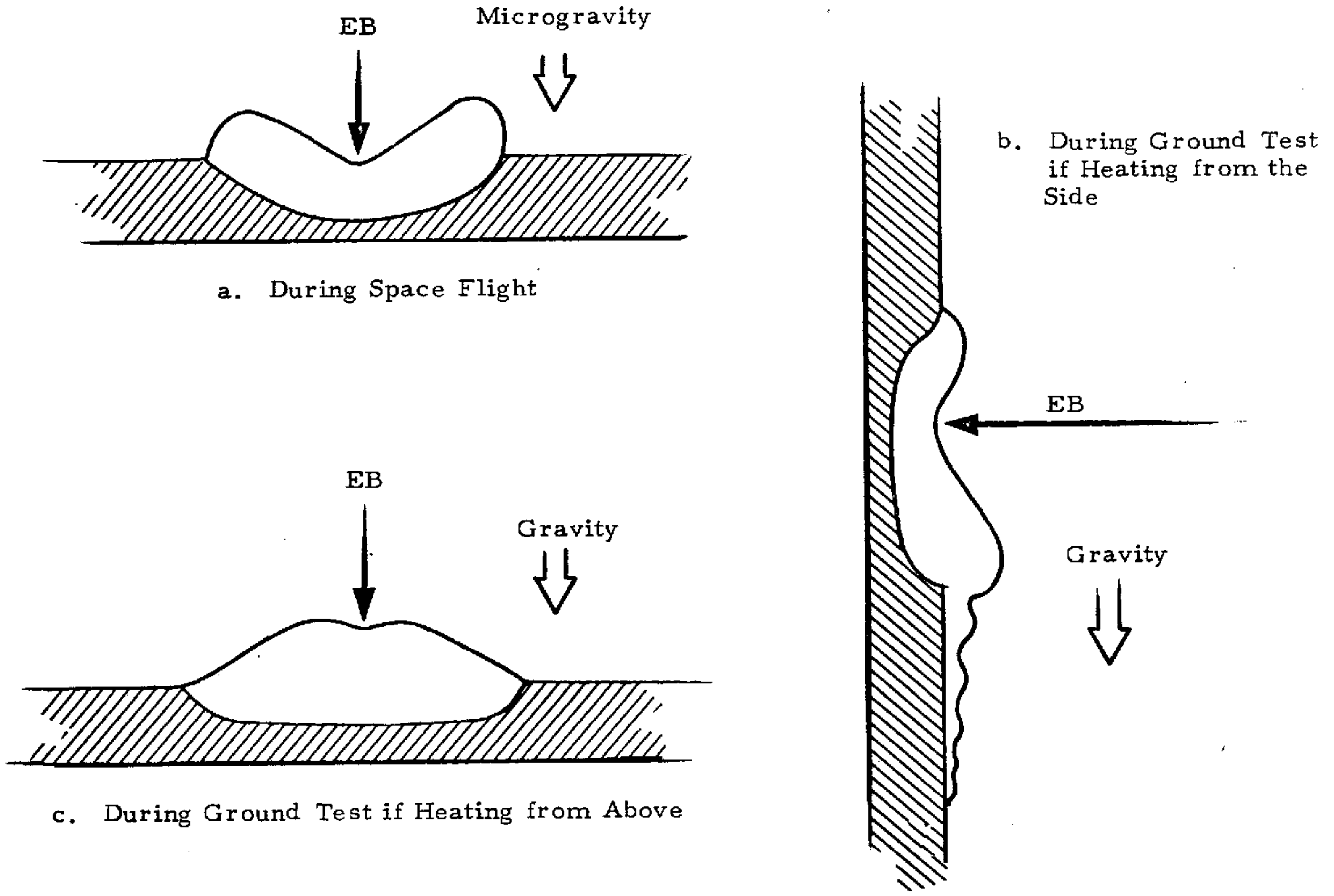

a. During Space Flight

b. During Ground Test if Heating from the Side

c. During Ground Test if Heating from Above

FIGURE 1. M551 DWELL POOL BEHAVIOR

Many of the microstructure examination results, however, have not been reported in time to be included in this report. In addition, visual observations of flight and ground samples were made to determine if beading and penetration changed significantly in space processing. Based on results reported to date, the following low gravity variations have been observed.

a. Surface condition: A significant difference was noted in surface appearance along the full penetration region of aluminum samples S/N 129 (Skylab) and S/N 130 (ground). The Skylab sample, in contrast to all previous ground samples, exhibited a bright center region free of oxide.

This result was not listed among the expected low-g variations because stirring was predicted to be similar for both terrestrial and Skylab processing. One explanation which has been proposed, however, involves transport of the lighter oxide from the back surface of the disk by gravity induced convection. While alternate explanations have not yet been proposed, the gravity-induced transport is open to several questions. First, the ground welds represent heating from the side. Thus the lighter oxide patches would tend to rise vertically and then carry over clockwise to the beam side (assuming the beam strikes the vertical plate from the right). Thermal convection currents, on the other hand, would be counterclockwise, thus opposing oxide density driven flow. Also the gravity induced stirring in this configuration should not be strong (see Appendix A.2), thus the transport time from the back to the front surface will probably be less than the time the metal remains molten. If sloshing rather than stirring is the dominant liquid mode, then mixing should be equal in space and on the ground (see Appendix B.3). Lastly, surface tension forces would have mixed the oxide in space if the beam-vapor cavity fully penetrates during this portion of the weld.

b. Dwell shape and penetration: As predicted in Section II-B, the gravity sag illustrated in Figure 1 was evident in the ground sample S/N 110 which also lead to more extensive dwell penetration than in the flight samples [5, pp. 21-23]. No "sag" was evident in the stainless steel flight sample S/N 106 as the dwell shape appeared similar to Figure 1a.

c. Convective motion: Examination of the 24 fps flight and ground movies for all three materials indicated agreement with the analytical predictions presented in Section II-A:

- Significant molten metal motion was exhibited in both the dwell and continuous weld molds for both ground and flight tests.

- Surface tension provided an equal magnitude of convection in the dwell pools in microgravity, but the filming speed was too slow to delineate flow patterns.

- No unstable splattering was evident even in the microgravity environment of Skylab.

d. Spiking frequency: No results have been reported to date on this characteristic of the stainless steel welds.

D. CONCLUSIONS

The primary conclusion which can be reached from the results now available is that no significant practical differences exist between terrestrial and microgravity electron beam melting. The differences found to date – oxide free front surface for the full penetration weld in the aluminum flight samples and the lack of gravity sag and shallower penetration in the stainless steel flight sample dwell – do not seem to have any practical benefits or detriments for conducting this operation in space. Although no results have been reported to date, the change in spiking frequency with gravity level and degree of melt superheat could lead to an increase in porosity and cold shuts in low gravity electron beam welding.

It is noted that the only other known low gravity electron beam welding experiments ever conducted [6] have come to similar conclusions using similar materials, beam parameters, chamber and disks, movie coverage and low-g aircraft experimentation. Their conclusions [6] were that not much difference existed between Earth and low-g specimens; aluminum rendered continuous beading, whereas stainless steel resulted in droplet beading; weld shape and penetration were the same on Earth and in low-g; and more porosity existed in one of the low-g specimens.

No quantitative evaluations could be made on the magnitude and pattern of flow in the dwells because filming speed was too low. This was true for both ground and flight tests.

SECTION III. M552 EXPERIMENT

The primary objectives of this experiment are to study and evaluate the capillary flow of molten braze material, to evaluate a tube joining technique for the assembly and repair of hardware in space, and to demonstrate the feasibility of exothermic reaction in space. The primary goal of this particular study is to predict the effects of gravity on capillary flow and capillary "gap" limits. Accounting for these differences in capillary flow and other space-versus-Earth processing differences (e.g., sedimentation, lack of hydrostatic pressure, vacuum, etc.), changes in braze solidification are to be estimated.

A. RESULTS OF PREFLIGHT ANALYSES

A summary of the most significant predictive results found are:

- Spreading time will be up to 50% shorter in gravity fields anticipated for Skylab than in ground tests.
- Molten braze alloy will always move to the narrow end of the variable gap samples due to capillary pumping action.
- Nucleation and orientation of secondary phases at the tube and sleeve will be more prevalent in the M552 narrow gap (less than 0.3 mm) samples than in the wider gap samples on both ground and flight tests. These effects should be more prevalent in the nickel plated specimens.
- The extent of capillary rise or spreading will be increased in zero gravity. This will be an especially significant result in cases where the capillary driving pressure has the hydrostatic pressure of the liquid column opposing it during terrestrial operations.
- The density ratio of silver to copper is $\rho_{Ag}/\rho_{Cu} = 1.2$, which means that silver may have a tendency to settle to the bottom of the joint on Earth, but would remain mixed on Skylab. Also, the density ratios of nickel and the braze alloy indicate that nickel may have a tendency to rise in joints on Earth, but would remain mixed on Skylab for the nickel plated specimens ($\rho_{Ni}/\rho_{Cu} = 1.02$).

- Turbulent or oscillatory laminar flow may occur for some gap widths in M552 Skylab processing, whereas only steady laminar flow would occur on Earth.

- Marangoni bubble migration can be important for M552 Skylab conditions, whereas buoyancy will control bubble location under terrestrial conditions. The Marangoni effect is a surface tension force which can drive fluid motion. It can arise from temperature or concentration gradients. In the present case, only temperature gradients are considered.

The detailed calculations and data upon which the preceding results were derived are given in Appendix C.

It is very important that the spreading time and fluid flow conditions be known in brazing. At first glance the flow analysis suggests that the time required to fill the joint is insignificant compared with the overall time of the brazing operation. This is not the case, however, when one considers rapidly occurring interactions such as alloying between the base and filler metal, differential rates of vaporization between the braze alloy constituents, and electrocapillarity (layers of ions alter the surface free energy of the filler).

These and other detrimental interactions, along with the importance of a knowledge of fluid flow conditions, are explored in detail by Milner [7]. Many of the important interactions with capillary flow in brazing operations are due to the presence of the fluxing agent. Fluxes remove the initial oxide film but may not entirely prevent further reoxidations. The use of a flux may also modify wetting and filling of a joint by:

- Electrochemical reactions between the base and filler metal with the flux acting as an electrolyte.

- Electrocapillarity in which layers of ions change the surface free energy.

- Substitutional chemical reactions in which an element of the flux is deposited on the surface of the base metal.

Alloying between the braze and base metal can radically affect joint filling by changing the surface tension, viscosity and melting point of the filler metal. Surface roughness can have an important effect as it may reduce a contact angle of up to 80 degrees down to zero. Surface roughness is also related by some to the important dynamic capillary effect known as contact angle hysteresis [8, 9]. The quicker the molten braze spreads, the less time there will be for the preceding interactions to significantly alter spreading.

B. EXPECTED LOW-G VARIATIONS

Using the preceding results and conclusions as a foundation, the following predictions can be made regarding the variations expected in the brazed joints processed in the microgravity environment aboard Skylab:

- The extent, rate and uniformity of spreading should be increased in low gravity which should lead to better joints. If turbulence occurs in wider gaps, this improvement may not be attained.
- The lack of hydrostatic pressure should allow a more symmetrical interface at the free surface of the filler and permit capillary spreading in wider gaps.
- The location of bubbles or voids should be different between Earth and Skylab processing and will depend on container orientation to gravity direction and the magnitude of effective gravity during the brazing operation.
- The settling of heavier components should not occur in microgravity.

The first item above is based on the premise that faster, laminar flow rates will allow less time for deleterious interactions to occur in the spreading molten braze.

The last three variations are directly dependent on the exact magnitude and direction of the gravity vector which will be operating during Skylab processing of M552. The magnitude of gravity aboard Skylab during the M552 experiment will be approximately 10^{-5} g_E (g_E = 9.8 m/sec), but the gravity direction is not yet known. Thus, precise predictions on bubble or void location cannot be given at the present time.

C. ACTUAL LOW-G RESULTS

Specific evaluations performed for this experiment in Phase C include:

- Examination of the extent and uniformity of spreading using data supplied by other investigators.
- Evaluation of the location of voids taking into account solidification shrinkage, buoyancy, Marangoni effect and the presence of the tube slot.
- Analysis of the microstructure data obtained by others especially near the free surface where surface tension convection might occur even in low gravity.

Based on results reported to date, the following low-gravity variations have been observed.

a. Spreading of braze alloy: Visual and metallurgical examinations indicate the molten braze alloy spread further and more uniformly in the constant gap Skylab samples, SLS-1, SLN-2 and SLS-3, than in the corresponding ground samples [10, 11]. A superior quality braze joint was noted in the SLS-1 sample [10]. Thus the predictions of improved capillary flow cited in Sections III-A and III-B and in Appendix C were confirmed. No firm conclusion can yet be reached on the absence or presence of turbulence during capillary spreading in microgravity. Turbulence was only expected to be possible in Skylab specimens SLS-3 and SLN-4.

b. Lack of hydrostatic pressure: A more symmetrical interface was noted in the meniscus of Skylab sample SNL-2. Spreading was more extensive in wide gap Skylab specimens SLS-3 and SLN-4 than in the corresponding ground samples [11]. These low-g variations agree with the predictions of Section III-B dealing with the lack of hydrostatic pressure in microgravity brazing.

c. Void location: In Skylab sample SLS-1 there was an absence of voids and porosity compared to ground specimens. This low-g variation could be attributed to the more uniform capillary spreading in microgravity. In Skylab sample SLN-4 porosity existed near the narrowest position of the gap which was not seen on ground based tests MCN-4, -5 and -6. This porosity has been attributed to solidification shrinkage, thus Marangoni bubble migration cannot be a factor. From thermal conduction considerations the axial ends should solidify before the center and the igniter end should solidify before the opposite end. Thus, porosity should be centered between the middle section of the braze alloy and the end opposite the igniter. The wide gap ground samples, however, would be influenced by thermal convection, as well as thermal conduction, and the last portion to solidify in these vertically processed specimens would have been the wide gap (upper) end. Thus ground specimens MCN-4, -5 and -6 would be expected to have less shrinkage induced voids near the narrow gap end than SLN-4, as actually occurred.

d. Distribution of components: Two significant low-g variations have been reported thus far: (1) increased nickel transport in the SLN-4 wide gap, and (2) complete radial mixing of the silver isotope in SLN-2 and SLN-4. Nickel distribution was greater in the wide gap area of flight specimen SLN-4 than it was in the variable gap ground samples MCN-4, -5 and -6 [10]. This increased nickel transport cannot be attributed to surface tension convection because $\sigma_{Ni} > \sigma_{Ag-Cu}$. Furthermore this mechanism, if possible, would have been operative on Earth also. Neither can gravity convection explain the increased Skylab nickel transport because $\rho_{Ni} \approx \rho_{Cu} < \rho_{Ag}$. This would cause nickel to rise to the wide gap area in ground samples MLN-4, -5 and -6. The preceding argument assumes that nickel is completely miscible in molten Ag-Cu. The phase diagram of Ag-Ni however, indicates a monotectic system with the possibility of two immiscible liquid phases if melt temperatures exceed 1435°C [12]. The silver-rich liquid is approximately 1.5 wt% Ni and the nickel-rich liquid is 3.65 wt% Ag. At the monotectic temperature the various molten components have the following densities:

Melt Component	Density at 1435°C (g/cc)
Copper	7.69
Ni-rich	7.81
Ag-rich	8.87

Thus the narrow gap in samples MCN-4, -5 and -6 would be depleted in nickel, and again gravity convection would not explain the increased nickel in the wide gap of SLN-4. In conclusion the low-g variation of increased nickel transfer in SLN-4's wide gap cannot be explained by surface tension or gravity effects and must therefore be due to some as yet unexplained phenomenon such as nucleation or solidification effects. It should also be pointed out that no quantitative information has been reported on M552 alloy distributions, only qualitative results.

Silver isotope tended to settle (Ag is densest component) in ground samples MCN-1, -2, -3, -4, -5 and -6; whereas this tendency was not reported in Skylab samples SLN-2 and SLN-4 [10]. As predicted in Section III-B, the ground based settling is due to gravity-induced sedimentation.

e. Braze-base metal reaction: As mentioned in Section III-A and Appendix C.4, the nucleation of nickel phases in the nickel plated samples, both ground and Skylab, should vary with gap width. This effect has been tentatively identified in SLN-2 [13] along with a possible gravity effect on this phenomenon. While the cause of this effect (surface energy considerations) should not vary with gravity, nickel transport variations due to gravity may have led to reported gravity variations in nickel-braze structure as well as reported gap size variations. The orientation of the nickel rich solid phase also seems to match the theories discussed in Appendix C.4 as the nickel-rich needles are perpendicular to the walls [13].

f. Microstructure: Different and/or unique microstructures were reported in Skylab samples SLN-2, SLS-4 and SLN-4. These low-g variations in microstructure are:

- SLN-2: A unique structure appeared in which a globular copper-nickel second phase is in a matrix silver phase with the globular phase present at between 30 and 90 volume percent. Also, a unique structure appeared in which a needle-like second phase, high in copper, is present in a silver matrix phase. The needles are perpendicular to the joint interface.

- SLS-3: The proeutectic silver-rich phase was more noticeable than in the ground samples and SLN-4 specimen.

- SLN-4: Altered copper structure in the narrow gap end when compared to ground samples. Presence of proeutectic silver-rich phase not found in ground samples.

Based on the qualitative nature of these results, these variations have been attributed to some unknown nucleation effects and not to convection effects.

g. Variable-gap capillary pumping: As expected (see Sections III-A, III-B, C.3), the melt in both the Skylab and ground-based variable gap samples SLN-4, MCN-4, -5 and -6 moved to the narrow end of the tube. No low-g variation was expected because capillary forces predominate in this configuration.

D. CONCLUSIONS

Three low-g variations in the M552 Skylab samples were successfully predicted based on expected variations in convection. These variations include: (1) increased extent, rate and uniformity of braze spreading in space with attendant improved joints (i.e., absence of voids in SLS-1); (2) lack of gravity sedimentation of the silver isotope in Skylab samples SLN-2 and SLN-4; and (3) increased voidage in the narrow gap of SLN-4. Unexpected low-g variations which could not be explained by differences in convection include: (1) increased nickel transport in the SLN-4 wide gap area; (2) different and/or unique microstructures in SLN-2, SLS-3 and SLN-4. Gravity independent results which were expected and confirmed by the Skylab results include: (1) the capillary pumping in variable gap samples which always sends the molten braze to the narrow end; and (2) the gap size effect on braze-base metal reaction. One unexpected result – the radial mixing of silver isotope in SLN-2 and SLN-4 – might be due to a difference in convection which is possible aboard Skylab. This variation in convection is the possibility of turbulent capillary spreading in microgravity, whereas only laminar capillary flow is predicted for ground samples.

SECTION IV. M553 EXPERIMENT

The basic objective of the sphere forming experiment is to determine the effects of reduced gravity on fundamental solidification phenomena. In particular, the following two effects should be predominent:

- The density difference between components (e.g., nickel and tin) will not lead to sedimentation as might occur in terrestrial operation.
- The specimens may be cast from the melt without using containers or molds (homogeneous nucleation).

The primary goal of this particular study is to delineate the magnitude and pattern of the molten metal flow for both terrestrial and space flight processing conditions. From a knowledge of the convective flow differences and the other differences between terrestrial and space processing, solidification theory will be utilized to predict how the grain structure, shape, internal voidage and surface finish of the spherical specimens should be affected. The "other" differences of space versus ground processing include changes in sedimentation and sphericity (lack of hydrostatic pressure and dominance of capillary forces in space) and possible differences in vibration, radiation, electromagnetic, and vacuum levels. The last four effects are not predictable to a precise degree of accuracy and are no doubt negligible in comparison to microgravity effects and are therefore not considered important.

A. RESULTS OF PREFLIGHT ANALYSES

A summary of the most significant predictive results found to date are given below.

- The following physical forces are operative on the M553 specimens during eb melting and solidification:
    - Gravity/Acceleration
    - Surface Tension
    - Lorentz (beam current)
    - Electrostriction
    - Magnetostriction
    - Electrostatic Charges
    - Solidification Shrinkage

  - Thermal Expansion
  - Vaporization
  - eb Mechanical Pressure Force

- Vigorous convective stirring occurs in the molten metal for each of the M553 sample materials. This fluid motion was exhibited on high speed motion picture film taken for ground tests and low gravity KC-135 aircraft tests.

- Both gravity and surface tension forces control molten metal flow during M553 ground tests. These natural convection driving forces arise because of severe non-isothermality during heating.

- Surface tension driven convection will occur in Skylab electron beam melting. In the near absence of gravity, the surface tension forces will provide an equivalent amount of convection aboard Skylab, but the flow pattern may be different from those of operations on Earth.

- Velocities of 20 cm/sec magnitude will be attained 0.1 sec after melting begins in the M553 nickel specimen (both for Skylab and ground tests). Fluid flow will decay 60 seconds after melting begins. This means that some degree of flow will exist upon freezing even for the free-floating M553 spheres.

- Very small and even negative pressures can be expected for the Skylab spheres due to outer shell shrinkage inducing tensions on the residual interior liquid.

- Shrinkage forces should lead to increased phase change induced convection in the Skylab M553 spheres.

- The mechanical pressure force associated with the impinging electron beam is not the cause of violent droplet breakup exhibited in some of the earlier KC-135 aircraft tests. Thus, any unstable splattering of the melt during heatup must be attributed to surface tension or electromagnetic instabilities at the melt surface or to degassing.

- Sedimentation will not be a factor in this experiment, because vigorous stirring will occur both in terrestrial and Skylab operations.

The preceding conclusions were drawn from examination of color motion picture film taken during ground and low-gravity aircraft flight tests and from detailed examination of the descriptive differential equations which govern eb melting and solidification. The equations were examined using dimensional analysis [3 and 4] and the nominal operating and boundary conditions for this experiment and the M512 chamber (Appendix A). Detailed derivations and results are given in Appendix D. Analysis of shrinkage pressures in residual liquid within spherical castings was abstracted directly from the literature [14].

B. EXPECTED LOW-G VARIATIONS

Based on the previous results and conclusions, the following predictions can be made regarding the variations expected in the specimens processed in the microgravity environment of Skylab:

- The primary differences expected in Skylab samples will be due to containerless casting; i.e., there will be no wall effects upon nucleation and solidification. Thus dendritic and grain structure should be finer because of the large degree of supercooling which can be obtained in homogeneous nucleation. Containerless, free suspension will also provide more perfectly spherical castings.

- Solidification shrinkage may induce imperfections in the sphericity of the castings. Furthermore, shrinkage may cause a number of voids or one large shrinkage cavity in the interior of each casting. The latter may occur symmetrically and form the basis for "hollow ball bearings."

- Finally, the residual fluid motion existing at the instant of freezing may introduce some inhomogeneity in the microstructure.

C. ACTUAL LOW-G RESULTS

Specific evaluations performed for this experiment in Phase C are given below.

- The flight film was examined and compared with KC-135 aircraft and ground test films to investigate differences in magnitude (velocity) of convection and flow patterns.

- The microstructure and grain size (obtained from other investigators) were examined for evidences of convective effects. Detailed evaluations based on these observations were limited because not all of the other investigators' results had been reported at the time of this writing.

Based on results reported to date, the following gravity observations are noted and discussed.

a. Fluid velocities and flow patterns: A compilation of fluid velocities (on the molten sphere surfaces) measured from movies taken during Skylab, KC-135 aircraft and terrestrial processing is shown in Table 1. These velocities were measured by tracking oxide or shiny contaminant patches as they moved over the molten surfaces both before and after complete melting. Several KC-135 measurements were obtained even after release from the ceramic pedastals. Shown in the table are the surface velocity, processing environment, gravity level, date of processing,filming information, specimen identification and time of measurement relative to the melting sequence. Beam power data for all measurements were approximately 50 mA and 20 kV. The velocity measurements are accurate to within 20%. The variations in results are probably due to differences in material compositions and beam settings (i.e., focus, impact point, voltage and amperage) rather than gravity effects.

As shown in Appendix D only surface tension and gravity forces are predicted to produce these velocities. The one velocity measurement obtainable from the Skylab movie was an order of magnitude lower than that obtained from some low gravity KC-135 aircraft and ground-based movies, but was similar to ground and KC-135 measurements also obtained long after complete melting. Thus it can be concluded that no significant difference in magnitude of convection occurred between Skylab, KC-135 and ground processing, which reinforces the theory of surface tension as the dominating force for fluid motion.

No information could be obtained on flow pattern variations in low-g because the slow filming rate of 24 frames per second used aboard Skylab could not delineate the flow profiles.

b. Metallurgical analysis: In addition to direct movie evidence of vigorous melt stirring, several other effects of convection were evident in metallurgical evaluations of Skylab specimens conducted by other investigators. The grain multiplication near the large shrinkage pore in the cap region of Skylab sample SL-1.6 (nickel-tin material) indicates vigorous flow probably due to solidification shrinkage [15]. Alumina was spread over the surface of SL-2.7 [16] a release-type nickel-tin specimen, which supports the existence of vigorous convective

Table 1

M553 SURFACE VELOCITY MEASUREMENTS

Processing Environment	Gravity Level* (g)	Date	Film (fps)**	Sphere Material	Fluid Velocity (m/sec)	Time of Measurement
Skylab	10^{-4}	6/15/73	Color, 24	Ni-Ag	0.02	Very long after melted
Ground	1	4/30/73	B&W, 3000	Ni-Ag	0.35 to 0.40	From early to complete melt
KC-135	$6 \cdot 10^{-3}$	7/25/72	Color, 200	Ni-Ag	0.20	Before full melt
					0.10	Right after full melt
					0.06	Long after full melt
Ground	1	10/20/72	B&W, 1000	Ni	0.15 0.20 0.33	Before complete melt
Ground	1	1972	Color, 200	Ni	0.12	Half melted

* $1g = 9.8$ m/sec^2

** fps = frames per second

stirring to transport the alumina from the pedestal. Similar findings of alumina transport were found on SL-1.8 [17], a nickel-copper specimen. Also most samples exhibited regions of equiaxed structure.

The metallurgical analyses of flight samples have, in general, exhibited a greater frequency or extent of independent nucleation or growth structures than do the ground samples [18]. In addition, the structures within these isolated areas are on a significantly finer scale than in similar areas of the ground based samples. These low-g variations agree with the predictions cited in Section IV-B.

c. Porosity: Several Skylab samples possessed a large spherical or oblong cavity. These large interior cavities were usually associated with a "cap region" opposite the flat, epitaxial side of the specimens. These large pores are no doubt produced by the large shrinkage forces predicted to exist during Skylab processing in Section IV-B and in Appendix D.5 and their appearance was expected.

D. CONCLUSIONS

The primary conclusion of the preceding discussions is that significant flow and stirring in the molten spheres (during and after eb melting) occurred in both terrestrial and space processing as predicted. The magnitude of this convective fluid motion was the same in both environments. The flow patterns, however, could not be quantitatively compared because the filming rate was too slow. Also, altered microstructure, increased grain refinement and the appearance of a single, large interior shrinkage pore have been found in the Skylab specimens as predicted in Section IV-B. These effects can be traced to a longer duration containerless freezing than in ground and KC-135 flights; i.e., the surfaces opposite the expitaxial nucleation site were cooler than in the non-Skylab specimens (assuming release). These surfaces nucleated much sooner than their non-Skylab counterparts, thereby entrapping a larger enclosed pool of residual liquid. The solidification shrinkage forces, which cause fluid flow and tensile stresses (increased shrinkage porosity), were therefore much greater in the Skylab specimens even though all of the samples appeared to have some degree of unplanned, heterogeneous nucleation (retainment of unmelted material or solidified prior to release).

It should be noted that a repeat of this experiment in the microgravity environment of space as is, except for longer, higher speed camera coverage, would yield much more hydrodynamic information. This information is important because hydrodynamics controls the release of the specimens and affects the solidification and microstructure properties. The release mechanism is of utmost importance because it will control the duration of free float time in the absence of acoustic or electromagnetic levitation. It is also recommended that a new experiment be performed with no active mechanical forces (springs) for release, i.e., allow only the vaporization and electromagnetic forces to initiate release. The slight forces could be counteracted by the small residual gravity field to yield very slow release acceleration and extremely long free-float times.

Further recommendations include the following additions to M553 experiment objectives.

- Study surface tension driven convection (due to non-uniform temperature) in free floating, molten spheroids. Similar types of fluid flow probably exist in stars such as the Sun, and this information should be of great interest to astronomers.
- Study the hydrodynamics and kinematics of deployment in zero-g. This step is critical for obtaining long periods of free float which will be essential to future space processing applications.
- Study the fluid dynamics involved in electron beam melting. Understanding of the stirring and heat flow associated with convective motions should be a valuable contribution to eb melting and solidification regardless of whether terrestrial or space applications are being considered.

REFERENCES

1. Bourgeois, S. V., and Grodzka, P. G.: Convection in Space Processing – Phase A Report, LMSC-HREC D306065, Lockheed Missiles & Space Company, Huntsville, Ala., July 1972.
2. Bourgeois, S. V.: Convection in Skylab M512 Experiments M551, M552 and M553: Phase B Report, LMSC-HREC TR D306697, Lockheed Missiles & Space Company, Huntsville, Ala., July 1973.
3. Churchill, S. W., and Hellums, J. D., Dimensional Analysis and Natural Convection, Chem. Engr. Prog. Symp. Ser. (Heat Transfer-Buffalo), Vol. 57, 1964, p. 75.
4. Ostrach, S.: Role of Analysis in the Solution of Complex Physical Problems, Third Intl. Heat Trans. Conf., Chicago, August 1966.
5. Report on Skylab M551 Samples, Batelle Memorial Institute, Columbus, Ohio, 24 September 1973.
6. Paton, B. E., Welding in Space, Welding Engineer, January 1972, pp. 25-29.
7. Milner, D. R.: A Survey of the Scientific Principles Related to Wetting and Spreading, Brit. Weld. J., March 1958, pp. 90-105.
8. Blake, T. D., and Haynes, J. M.: Contact Angle Hysteresis, Progress in Surface and Membrane Science, Vol. 6, 1973, pp. 125-138.
9. Rose, W., and Heins, R. W.: Moving Interfaces and Contact Angle Rate Dependency, J. Colloid Sci., Vol. 17, 1962, pp. 39-48.
10. Williams, J. R.: 90-Day Report – Skylab Experiment M552, NASA-George C. Marshall Space Flight Center, Huntsville, Ala., 12 October 1973.
11. Visual Observation of M552 Skylab Specimens and Hardware During NDT at MSFC, NASA-George C. Marshall Space Flight Center, Huntsville, Ala., 17 July 1973.
12. Hansen, M.: The Constitution of Binary Alloys, McGraw-Hill, New York, 1958, pp. 36-37.
13. Report on Skylab M552 Samples, Batelle Memorial Institute, Columbus, Ohio, 21 September 1973.

14. Campbell, J.: Hydrostatic Tensions in Solidifying Materials, Trans. Met. Soc., AIME, Vol. 242, 1968, p. 264.

15. Kattamis, T. Z.: Investigation of Solidification in Zero-Gravity Environment: M553 Sphere Forming Experiment, 90 Day Progress Report, Contract NAS8-28734, University of Connecticut, Storrs, Connecticut, 15 September 1973.

16. Johnson, P. C., and Peters, E. T.: M553 Sphere Forming Experiment 90 Day Report, Contract NAS8-28723, A. D. Little, Inc., Cambridge, Mass., October 1973.

17. Brown, J. L., Report on Preliminary Examination of Skylab Samples from the M553 Sphere Forming Experiment, NAS8-28735, Georgia Institute of Technology, Atlanta, Ga., 25 September 1973.

18. Ninety-Day Interim Report on Evaluation of M553 Sphere Forming Specimens Processed in Skylab 1/2, NASA-George C. Marshall, Huntsville, Ala., 12 October 1973.

APPENDIX A

ENVIRONMENTAL CONDITIONS FOR THE SKYLAB M512 CHAMBER

In this appendix a compilation is presented of pertinent environmental conditions for the M512 experiments to be performed aboard the first Skylab mission. Also included is a summary of convection sensitivity calculations for the M512 experiments and a general discussion on the effects of convection and homogeneous nucleation on solidification.

A.1 M512 OPERATING CONDITIONS

The M512 facility will contain several experiments (M551, M552, M553, M566) for the investigation of melting and solidification in a space environment. Convection in the molten fluid may be a controlling parameter in these processes. In order to evaluate convection and other phenomena, the pertinent environmental conditions of each experiment must be known. This appendix contains a compilation of the factors that are important for assessing convection.

The environmental conditions expected for each experiment are shown in Table A-1. Data enclosed within parentheses indicate that they are estimates and need further study. Also some categories have no data which indicates that these factors could not be estimated with any accuracy.

A.2 CONVECTION SENSITIVITY

Dimensionless ratios which give an indication of convection sensitivity for each M512 experiment are shown in Table A-2. These numbers were evaluated by estimating pertinent temperature gradients from documented ground-base studies, Brown Engineering thermal analyzer studies and Lockheed thermal studies and utilizing the data in [A.1]. The table contains Rayleigh numbers (Ra), Marangoni numbers (Ma), thermal diffusivities (α), Prandtl numbers (Pr), and Stefan numbers (St) which have been obtained for the molten metals in the M551, M552, M553 and M566 experiments. Critical Rayleigh (Ra_c) and Marangoni (Ma_c) numbers for these experiments were estimated from the literature [A.2, A.3 and A.4]. When the Rayleigh number exceeds its critical value, gravity-induced convection will occur and significantly affect heat transfer. Similarly, if the critical

Table A-1
ENVIRONMENTAL CONDITIONS FOR M512

<table>
<tr><th>Condition</th><th>M551</th><th>M552</th><th>M553</th><th>M554</th></tr>
<tr><td>Date/Time of Experiment</td><td colspan="4">5/8/73</td></tr>
<tr><td>Gravity Level (cm/sec^2)</td><td colspan="4">(.001 - .1)</td></tr>
<tr><td>Gravity Gradient (1/sec^2)</td><td colspan="4"></td></tr>
<tr><td>Initial Chamber Pres. (atm)</td><td colspan="4">(0.34)</td></tr>
<tr><td>Initial Atmos. Composition in Chamber (wt %)</td><td colspan="4">(O_2(70), N_2(30)</td></tr>
<tr><td>Initial Chamber Temp. (°C)</td><td colspan="4">(10 - 32)</td></tr>
<tr><td>Electron Beam</td><td></td><td></td><td></td><td></td></tr>
<tr><td>• Wattage</td><td>1.6 kW</td><td></td><td>(1.2 kW)</td><td></td></tr>
<tr><td>• Amperage</td><td>80 mA</td><td></td><td>50-60 mA</td><td></td></tr>
<tr><td>• Focus</td><td>.08 - .23 cm.</td><td></td><td>.64 cm</td><td></td></tr>
<tr><td>• Duration</td><td>15 - 30 sec</td><td></td><td>3-5 sec/sphere</td><td></td></tr>
<tr><td>• X-ray level</td><td>(> 20 μrad/sec)</td><td></td><td>(>20 μrad/sec)</td><td></td></tr>
<tr><td>Magnetic Field Level</td><td></td><td></td><td></td><td></td></tr>
<tr><td>Vibration Levels</td><td></td><td></td><td></td><td></td></tr>
<tr><td>• Amplitude (cm)</td><td></td><td></td><td></td><td></td></tr>
<tr><td>• Frequency (Hz)</td><td></td><td></td><td></td><td></td></tr>
<tr><td>Electrical Fluctuations</td><td></td><td></td><td></td><td></td></tr>
<tr><td>Wheel Rotation</td><td></td><td></td><td></td><td></td></tr>
<tr><td>• Rate (rpm)</td><td>2.5 ± 0.1</td><td></td><td></td><td></td></tr>
<tr><td>• Radius (cm)</td><td>8.25</td><td></td><td></td><td></td></tr>
<tr><td>• Weld Radius (cm)</td><td>6.04</td><td></td><td></td><td></td></tr>
<tr><td>Cabin Conditions</td><td></td><td></td><td></td><td></td></tr>
<tr><td>• Temperature (°C)</td><td colspan="4">20 - 25</td></tr>
<tr><td>• Pressure (atm)</td><td colspan="4">0.34</td></tr>
<tr><td>• Composition (wt %)</td><td colspan="4">O_2(70), N_2(30)</td></tr>
<tr><td>Space Atmosphere</td><td></td><td></td><td></td><td></td></tr>
<tr><td>• Temperature (°C)</td><td colspan="4">950 - 1160</td></tr>
<tr><td>• Pressure (torr)</td><td colspan="4">10^{-6} - 10^{-8}</td></tr>
<tr><td>• Composition</td><td colspan="4">10^6 e/cc, 10^8 neut. particles/cc, MW = 20-26</td></tr>
<tr><td>Chamber Size</td><td></td><td></td><td></td><td></td></tr>
<tr><td>• Volume:</td><td colspan="4">$4.25 \cdot 10^{-2}$ m^3</td></tr>
<tr><td>• Diameter:</td><td colspan="4">0.42 m</td></tr>
<tr><td>Size of Valve to Space:</td><td colspan="4">0.1 m vent valve (1.0 m long tube to space)</td></tr>
</table>

Table A-2

SENSITIVITY ANALYSIS OF M512 EXPERIMENTS

Material	Ra$_c$	Ra (10^{-4}g)	Ra (lg)	Ma$_c$	Ma	α (cm^2/sec)	Pr	St
2219 Aluminum (Continuous Weld)	1500	10^{-4}	1.0	80	1.3	0.325	0.015	2 x 10^{-4}
321 SS (Dwell)	1500	5.7	57,400	80	236,000	0.165	0.046	4 x 10^{-2}
Tantalum	1500	——	——	80	——	0.155	0.013	4 x 10^{-2}
Braze Alloy	1700	10^{-2}	62	——	800	0.202	0.021	——
Nickel	700	.24	2,370	200	12,900	0.120	0.054	2 x 10^{-3}
Ni-Sn	700	.21	2,130	200	5, 530	0.130	0.043	2 x 10^{-3}
Ni-Cu	700	.15	1,480	200	5, 750	0.125	0.048	4 x 10^{-3}
Aℓ-Cu Eutectic	90	.19	1, 900	~1000	7, 000	0.284	0.019	——

Marangoni number is exceeded, surface tension-driven convection will occur. The Stefan number is useful in analyzing radiative cooling (M551 and M553) and the thermal diffusivity and Prandtl number are useful in studying thermal profiles and fluid motion. Table A-3 represents a quick comparison of the modes of convection expected in M512 experiments on Earth and on Skylab.

It must be emphasized that the critical conditions only rigorously apply when gravity is aligned with and opposed to the temperature gradient. It is also assumed that uniform heating exists (linear temperature gradient) and that temperature gradients only occur in one direction. With the exception of M566, these conditions are not met on these M512 experiments, but more rigorous analyses have not appeared in the literature. With these rather severe restrictions in mind, the conclusions in Table A-3 give an approximate indication of the convection modes which can be expected for these experiments.

No values for Ra and Ma are shown for tantalum because a reliable estimate of tantalum's thermal conductivity in the molten state has not yet been found. Similarly the critical Marangoni numbers for M566 and M552 are not given because Ma_c has not been estimated in the literature for such large aspect ratio configurations. Values of the Stefan number for these two experiments are not given because melt radiation will not be a factor.

The Rayleigh number, Ra, is the weighted ratio of the buoyancy driving force to the viscous forces which tend to resist fluid flow and is defined by,

$$Ra = \frac{gd^3 \beta \Delta T}{\nu \alpha}$$

where g is the gravity acceleration, d the depth of the fluid layer, β the thermal volumetric expansion, ΔT a temperature difference in the fluid, ν the kinematic viscosity, and α the thermal diffusivity. A corresponding number of surface tension force to viscous force is given by the Marangoni number:

$$Ma = \frac{\frac{\Delta\sigma}{\Delta T} \Delta T \, d}{\rho \nu \kappa}$$

where $\Delta\sigma/\Delta T$ represents the rate of change of surface tension with temperature and ρ the density.

Table A-3

GRAVITY AND SURFACE TENSION CONVECTION IN M512 EXPERIMENTS

Experiment	Material	Gravity-Driven		Surface Tension-Driven
		1g	10^{-4}g	
M551	2219 Aℓ (Rotating Disk)	No	No	No
	321 SS (Dwell)	Yes	No	Yes
M552	Ag-Cu Braze Alloy	No	No	No
M553	Nickel	Yes	No	Yes
M554	Aℓ-Cu	Yes	No	Yes

A.3 CONVECTION EFFECTS ON SOLIDIFICATION

Inhomogeneities which are usually present in solidified metals can be classified as occurring either on the microscopic or macroscopic scale. An example of a microscopic defect is dendritic segregation. Fluid flow usually has little direct effect on these microscopic inhomogeneities, but can have major influence on macrosegregation and other macroscopic properties [A.5 and A.6]. Some of these defects are shown concisely in Figure A-1 which illustrates convection derived influences on normal and inverse macrosegregation, banding, nonplanar solid-liquid interfaces, and grain enhancement. Sources of convection considered to produce the defects of Figure A-1 are: volume contraction on solidification ($\rho_L \neq \rho_S$); flow due to second phase nucleation ahead of the advancing solidification front; and buoyancy-driven thermal and solutal (heavier solute sinks) convection. Other sources of fluid flow which have received little attention are electromagnetic stirring, vibrations and surface tension-driven thermal and solutal convection. The effects of these three sources of flow will be somewhat similar to those of buoyancy-driven convection.

Solidification shrinkage induced flow has two effects on solidification. First, the inrushing melt has a strong effect on the temperature distributions at a solid/liquid interface [A. 7]. Secondly, solute rich liquid in the interdendritic spaces and at the macroscopic growth interface are drawn toward the solidus resulting in high-concentration solid near the heat sink. This is the reverse of usual distribution of impurity and has been termed inverse segregation.

Nucleation induced macrosegregation can be traced to the settling or rising of phases having differeing densities when a strong gravity field is present. Primary phases which nucleate ahead of the main growth interface are denser than the bulk metal and settle; while bubbles, oxides and carbon-rich phases may float. Crystal settling may also be responsible for the "V-defect," which can be described as lines of segregation toward the bottom or central portions of castings. Also in low temperature gradient dendritic growth, dendrites may become sufficiently large that they cannot support their own weight and the entire group may sag.

Thermal, buoyant convection is capable of inducing high (tens of cm per sec) fluid velocities [A.5]. The rapid flow can sweep away solute rich liquid from the interface and thus produce positive segregation. The fluctuations in temperature usually associated with convection in metallic liquids may detach portions of a dendrite and be transported elsewhere by the general flow (grain multiplication). A final defect associated with thermal flow is banding where alternating layers of solute-poor and solute-rich material are present. Bands

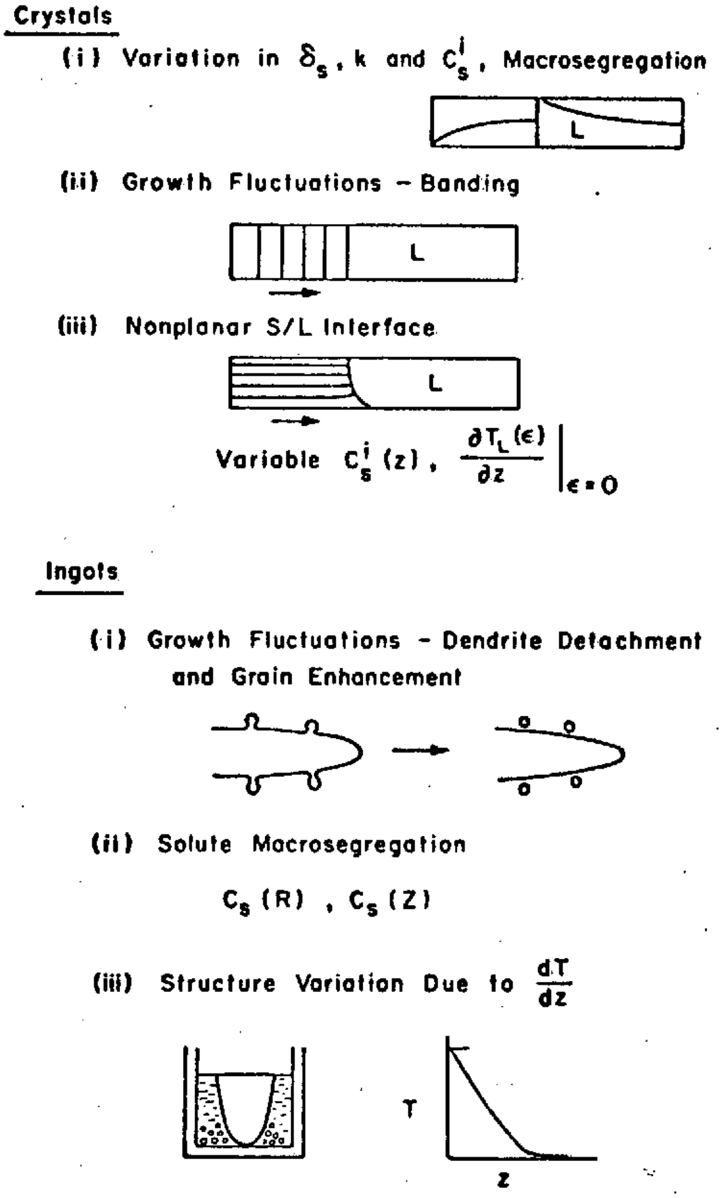

FIGURE A-1. EFFECTS OF CONVECTION ON SOLIDIFICATION [A.2] can be formed when a thermal convective "pulse" contacts the interface inducing a change in the freezing rate and a subsequent change in the composition at the solid/liquid interface.

Solutal convection may be more extensive than thermal convection in complex alloys. Excess solute rejected into interdendritic regions will rise or fall depending on the density difference. Of pertinence to the M551 and M566 experiments, large regions of copper-rich material may be expected near the bottom of Aℓ-Cu alloys [A.8]. The flow may be strong enough to detach entire portions of a dendrite and carry them away. This occurs most frequently when there is a long two-phase region (wide melting range), which produces fragile dendrite arms. The regions of different composition which are produced by this type of convective flow may be up to a centimeter in diameter and are called freckles. Extensive microsegregation is associated with this defect. The forces exerted on fragile dendrites can also form channels through which high concentration liquid can flow producing regions of high concentration solid termed "A-segregates."

From the preceding discussion it is seen that defects and inhomogeneities in the solidified product are associated with convection in the melt. Thus reduction or elimination of buoyant convection by space processing should lead to more homogeneous castings, crystals and welds, and attendant improvements in the mechanical and physical properties of these products.

A.4 HOMOGENEOUS NUCLEATION EFFECTS

Microgravity solidification in the M553 experiment may lead to containerless freezing which offers the probability of homogeneous nucleation and attendant large degrees of undercooling. Most of the effects of large undercooling, and thus extremely rapid freezing rates, are beneficial. Increasing the amount of undercooling in an alloy leads to substantial reductions in both the segregation ratio of alloying elements and of dendrite-arm spacings. As a consequence, the rate of homogenization of an alloy increases with increasing undercooling. Other beneficial effects of undercooling are reduction in grain size, refinement of endogenous inclusions such as silicates and sulfides, and homogeneous distribution of porosity. All these factors are beneficial to mechanical and possibly physical properties of an alloy.

REFERENCES

A.1. Bourgeois, S.: Environmental Factors and Physical Properties for M551, M552, M553 and M554, LMSC-HREC D306001, Lockheed Missiles & Space Company, Huntsville, Ala., June 1972.

A.2. Samuels, M. R., and Churchill, S. W.: AIChE J., Vol. 13, 1967, p. 77.

A.3. Baldwin, P.: Convection in Fluid Sphere Containing Heat Sources, Proc. Camb. Phil. Soc., Vol. 63, 1967, p. 855.

A.4. Pearson, J. R. A.: On Convection Cells Induced by Surface Tension, J. Fluid Mech., Vol. 4, 1958. p. 489.

A.5. Cole, G. S.: Inhomogeneities and Their Control via Solidification, Met. Trans., Vol. 2, 1971, pp. 357-367.

A.6. Cole, G. S.: Transport Processes and Fluid Flow in Solidification, Chapter 7 in Solidification, American Society for Metals, Metal Park, Ohio, 1971, pp. 201-274.

A.7. Cambre, A.: On the Dynamics of Phase Growth, Quart. J. Appl. Math., Vol. 9, 1956, p. 224.

A.8. Mehrabian, R., Keane, M., and Flemings, M. C.: Interdendritic Fluid Flow and Macrosegregation; Influence of Gravity, Met. Trans., Vol. 1, 1970, p. 1209.

APPENDIX B

DETAILED ANALYSES FOR THE M551 EXPERIMENT

This appendix contains detailed results of theoretical calculations for the M553 experiment. The first section contains an analysis of the driving forces, magnitude and pattern of natural convective fluid flows which occur in the Metals Melting Experiment. This section is followed by a discourse on the possibility of molten pool spattering due to the momentum of the impinging electron beam. Finally the spiking in the partial penetration zone of the stainless steel samples is evaluated for gravity effects.

B.1 CONVECTION ANALYSIS

Summary

Results of the convection analysis indicate that: (1) surface tension is the main driving force for fluid motion in microgravity electron beam welding; (2) gravity forces also predominate in ground-based welding; (3) vapor pressure is the primary cause of surface deflection (cutting action); (4) spiking frequencies in the stainless steel Skylab samples should be increased as much as 25%; and (5) fluid dynamics undoubtedly control the mixing, microstructure, and shape of the weld pool in the electron beam weldings.

Dimensional Analysis

As in the other M512 experiments, the fluid dynamics of the M551 experiment is the most important factor in determining quality of the final product (in this case, the solidified pool, seam and cut produced on various areas of thin metal disks). Flow patterns in the molten material are important in these experiments, because all of the materials have low entropies of fusion [B.1]. Thus, their solidification (microstructure) is controlled by the rate of heat transfer removal [B.2], which changes with the flow field [B.3 and B.4]. The flow will be especially important in the dwell mode, since a relatively large pool of melt will be created. The degree of flow will also determine the amount of mixing attained. If no or little flow were present, all heavier components would segregate to the bottom of weld zones on earth, but to a much lesser extent in microgravity environments. Fluid flow can also affect the shape of the weld pool [B.7].

Application of dimensional analysis [B.5 and B.6] to the governing equations for eb welding, coupled with ground-based and KC-135 experiments, should enable prediction of the extent of reduction or increase of motion in the weld pool and/or the change in flow pattern in electron beam welding in space. Possible physical forces which could induce fluid flow in the M551 experiment, and their causes, include:

- Effective Gravity Force: Resultant force on weld specimen due to earth's gravity and centrifugal and coriolis forces of orbiting spacecraft.
- Lorentz Force: Electromagnetic forces induced by passage of the electron beam current through the specimen.
- Electrostriction: Stresses induced when electrical permittivity changes with density.
- Magnetostriction: Stresses induced when permeability changes with density.
- Electrostatic Force: Caused by presence of excess electrical charge (due to beam current and/or thermionic emission).
- Surface Tension: Tangential stresses at vapor-liquid or liquid-liquid interfaces can be induced if surface tension depends on temperature and/or concentration. Surface tension will also cause pressure gradients across curved interfaces.
- Density Differences Accompanying Phase Changes
- Beam Force: Impinging electrons give up their momentum.
- Thermal Expansion: Dilation and compression of fluids whose density changes appreciably with temperature can induce fluid flow.
- Vibration: Uncontrolled movement due to engine operation, astronaut motion, particle impacts, etc.
- Centrifugal and Coriolis: Generated by disk rotation.
- Vapor Pressure: Evaporating molecules impart momentum which leads to normal stresses at vapor-liquid interface.

- Inertia Forces: Tend to sustain induced motions.
- Viscous Forces: Tend to resist driving forces.

The preceding forces, which could influence fluid flow and solidification, appear explicitly in the conservation equations which apply to formation of a molten pool by electron beam heating. These equations are given in detail in Appendix D.

A formal method of determining the controlling physical forces affecting fluid flow and solidification in electron beam welding was introduced in Appendix D. The controlling physical forces are determined by nondimensioning the governing differential equations and performing an order-of-magnitude comparison on the various dimensionless groups which result. The key to successful analysis is in choosing the proper reference values; i.e., since no freestream velocity exists, which forces do we equate to estimate a "characteristics" or "typical" velocity. Choosing the proper characteristic velocity is very important, since the reference time, temperature, etc., usually depend on this velocity. The results arrived at in Appendix D are also considered valid for the M551 experiment.

The equation, in dimensionless form, governing electron beam melting is Equation D.1 shown in Appendix D. Values of the pertinent dimensionless groups for each of the M551 materials are given in Table B-1. Examining Table B-1 in conjunction with Equation D.1, an order-of-magnitude analysis indicates that surface tension driven convection will occur both in ground tests and for Skylab conditions because $N_{Oh} << 1$. Furthermore, gravity driven convection will exist on ground tests, but will be negligible in the reduced gravity of Skylab. Thus different forces will control convection on earth versus Skylab. The preceding analysis also indicates that electromagnetic or Lorentz forces will be negligible with regard to causing fluid motion. See Appendix D for further details.

A review of the literature on electric arc welding, which is somewhat similar to electron beam welding, has generated the following facts which can be compared to the preceding conclusions. In a study of motion in weld pools in arc welding, Woods and Milner [B.7] conclude that Lorentz forces are the primary cause of motion. An additional secondary cause is the momentum imparted by the impinging arc. Surface tension forces were not considered. Kotecki et al [B.8] showed that surface tension and momentum forces of the impinging arc controlled ripple formation in gas tungsten arc welds. Surface tension controls when the arc is shut off. Brimacombe and Weinberg [B.9] also conclude that surface tension is the driving force for fluid motion once the impinging jet is removed.

Table B-1
M551 DIMENSIONAL ANALYSIS

Material	N_{Oh}	N_{Bo}	$\frac{1}{N_{Oh}}$	$\frac{N_{Bo}}{N_{Oh}}$*	$\frac{N_{Bo}}{N_{Oh}}$†
2219 Aluminum	5.8×10^{-4}	3.09	1713	5287	0.53
321 Stainless Steel	6.3×10^{-4}	1.56	1581	2461	0.25
Tantalum	3.4×10^{-4}	7.19	2942	21150	2.11

*With Earth gravity (9.8 m/sec^2)

†With 10^{-4} Earth gravity

One direct result of formulating the governing equations is that surface deflection (cutting action) is primarily caused by vapor pressure, but that the beam force is also appreciable. This was determined from the vapor-liquid force equation of Appendix D, which indicates that,

$$\frac{\text{Vapor Pressure}}{\text{Beam Pressure}} \approx 2$$

This agrees with earlier studies [B.10].

Flow Patterns

The aforementioned difference in controlling forces between terrestrial and space processing for the M551 experiment should result in altered flow patterns between these two conditions. From a knowledge of flow patterns generated by surface tension versus buoyancy controlled convection on Earth [B.11], the situation illustrated in Figure B-1 would no doubt exist during melting on Earth, while that shown in Figure B-2 would prevail in space. These two figures represent cross-sectional views through the molten dwell pool. The pattern shown in Figure B-2 is based on the fact that surface tension is stronger in cooler regions; therefore the coolest portion of the specimen will exert the strongest "pull" on the surface. In both cases, the motion is termed cellular [B.11].

These predicted flow patterns have been verified by M551 ground tests. Movies taken during ground-based tests of the M551 experiment for all three materials (2219 aluminum, stainless steel and tantalum) were studied during the week of 16 March 1973. The quality of the film and the resolution of the fluid flow in the weld pool were excellent in several of the tests. Four distinct Benard convection cells were observed in the weld pool of a stainless steel dwell. Significant molten metal motion was exhibited in each of the specimens filmed in both the dwell and weld (disk rotating) modes.

B.2 WELD POOL SPLATTERING

In both the M551 and M553 experiments, the heat released to the metal specimens by the impinging electron beam enables a molten pool to form. A question arises as to the stability of these molten liquids in low gravity. At least one of the KC-135 M553 specimens was seen to break up violently into many smaller liquid spheroids upon complete melting. The electron beam was still hitting the specimen during break up. A similar instability might develop in the molten puddle formed during the dwell mode of the M551 experiment,

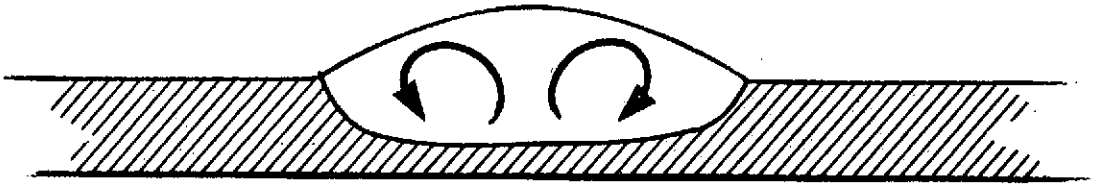

FIGURE B-1. CONVECTIVE PATTERN IN M551 DWELL POOL MELTING ON EARTH

FIGURE B-2. CONVECTIVE PATTERN IN M551 DWELL POOL DURING MELTING IN SPACE wherein the liquid might not adhere and separate from the solid disk (violent splattering).

There are at least three different mechanisms which might explain the instability observed in the M553 KC-135 specimens. Upon melting, the specimen may have experienced violent degassing which could have led to droplet breakup. Another mechanism might be electrohydrodynamic instability caused by interactions between the electromagnetic forces of the electron beam and the fluid flow field set up in the molten metal by both thermal gradients, Lorentz and other forces [B.12]. Lastly, the momentum force associated with the impinging electron beam might have set up unstable surface oscillations on the molten metal.

The latter instability mechanism has been treated recently by Berghmans [B.13]. He performed a theoretical study of fluid interface stability with special attention being given to the role of surface tension. It was motivated by its possible application to the splattering of molten metal as observed during electric arc welding.

Berghmans' study concluded that the weld pool interface would be stable if the following condition was met,

$$\mathrm{We}^2 \leq 1.04 + 3.3\ \mathrm{Bo}^2 \qquad (B.1)$$

where

We = Weber number

Bo = Bond number

The analysis is only rigorous if inertia and viscous effects are small compared to surface tension effects. Inertia effects are not negligible in the M551 and M553 experiments, but the results of Berghmans' study should give a reasonable approximation.

The criterion expressed by Equation (B.1) was applied to each of the materials in both the M551 (2219 aluminum, stainless steel, and tantalum) and the M553 (pure nickel, Ni-Cu, Ni-Ag, and Ni-Sn) and for gravity levels between ground tests ($g_E = 980\ \mathrm{cm/sec}^2$) and those of Skylab ($g = 10^{-5}\ g_E$). Beam diameter was also varied between 0.635 and 0.07 cm. For each of the above cases,

$$\mathrm{We}^2 < 10^{-2}$$

therefore, the momentum force of the electron beam will not be a primary cause of weld pool instability in either M551 or M553.

B.3 GRAVITY EFFECTS ON SPIKING

The electron beam welding phenomenon known as spiking occurs in the partial penetration welds of the stainless steel samples in the M551 experiment. This phenomenon is illustrated in Figure B-3 which indicates that spiking is caused by oscillation of the melt. Using a pinhole X-ray camera [B.14] and radiographs of beam-on-plate welds [B.15] to reveal beam-metal interactions in the cavity of an electron beam weld, the following mechanism can be proposed for spiking:

> "With initiation of the beam, the beam vaporizes the material as it bores its way into the material. Full penetration is reached within 50 millisec with the establishment of an equilibrium cavity. The beam, impinging on the cavity base, boils heated liquid up the walls of of the cavity, most likely in a whirling fashion. Complete metal mixing results due to this dynamic pumping action. Cavity closures are produced as the metal loses kinetic energy. Once a closure forms, it intersects the electron beam producing two effects. First, while the beam is heating the closure, regions below the closure are given time to cool. Second, the closure is heated and generally falls back into the cavity and the cycle recurs. However, the closure may occasionally be vaporized in an explosion. After closure explosion, the cavity is clear of liquid and the beam is again free to impinge on the cavity base causing a spike. However, much more frequently the closure falls back into the cavity. This cyclic mechanism continues (at a typical rate of 150 cycles per sec) as an equilibrium process.
>
> "Spiking results when there is a failure or interruption of the cyclical closure-fallback mechanism. When a closure fails to materialize or is exploded out, the electron beam is free to dwell on the cavity base for a longer time, thus producing a penetration spike." [B.14]
>
> "A spike is formed each time the electron beam penetrates to the base of the weld and the severity of the spiking depends on the frequency of the oscillation and the welding speed as well as the material being welded.
>
> "When the molten metal flows into the cavity, it can easily trap bubbles of contaminant gases at the base of the weld and, if the cooling rate is sufficiently rapid, the fluid may freeze before the gases can be convected to the surface, thus giving rise to porosity in the fusion zone. Similarly, if the cooling rate is sufficiently rapid,

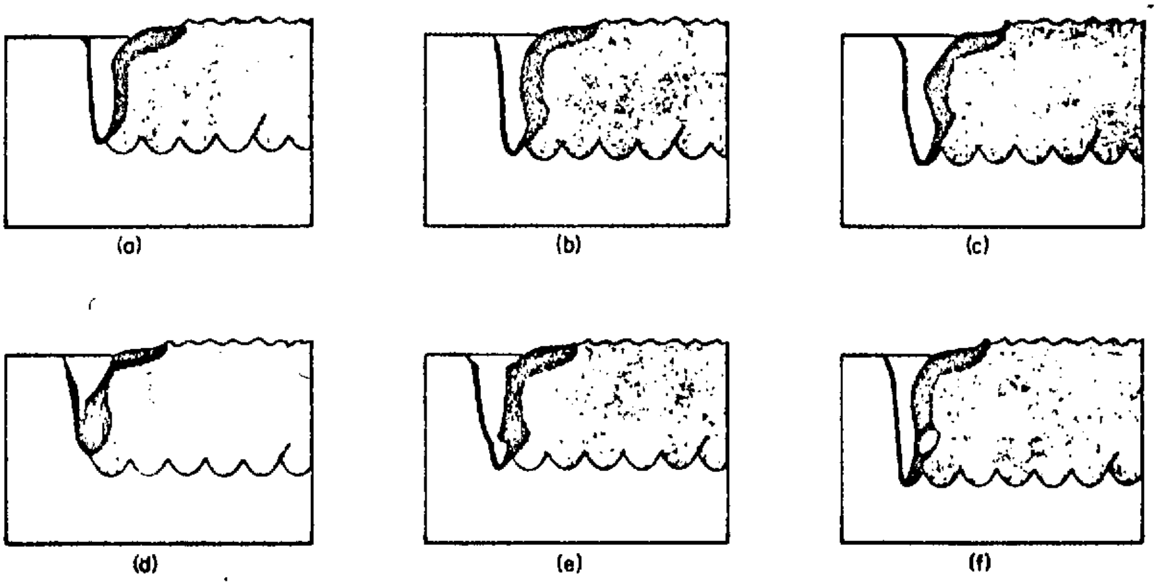

FIGURE B-3. SPIKING MECHANISM IN ELECTRON BEAM WELDING [B.15] then the melt, as it falls into the cavity, may interrupt the beam long enough for the walls of the spike to freeze so that the fluid, upon falling into the spike, might not bond, thus forming a cold shut or crack.

"The alternate penetration and closing of the cavity are also very efficient in mixing the melt and results in a very homogeneous fusion zone." [B.15]

A theoretical analysis of the melt-beam dynamics described above and in Figure B-3 shows that spiking frequency is predicted by Reference B.15.

$$\omega = \frac{\frac{1}{4}\sqrt{\frac{g}{h}}}{\left[\sqrt{\frac{P_V - \frac{2\sigma}{a}}{\rho g h}} - \sqrt{\frac{P_V - \frac{2\sigma}{a} - \rho g h}{\rho g h}}\right]} \qquad \text{(B.2)}$$

where

h = maximum depth of penetration

$2a$ = weld width

g = gravity level

P_V = vapor pressure of molten metal

σ = surface tension of molten metal

ω = spiking frequency

The preceding analysis considered welding a horizontal plate from above. The configuration utilized for M551 ground tests (beam impinges vertical plate from the side at a nine o'clock position with clockwise rotation of the plate past the immobile beam) also lends itself to cavity oscillations as the trailing melt tends to be above the beam. It should also be pointed out that the above oscillation frequency represents the natural frequency of the cavity. A lower frequency, superimposed over the natural frequency, may occur due to an interaction of the static cavity closing forces (hydrostatic head and surface tension) and the dynamic forces. The dynamic forces arise from the motion of the wave or ripple which is formed in the melt as the cavity penetrates.

Thus Equation (B.2) should not be expected to generate exact, rigorous results to match actual M551 experimental data. It can, however, be utilized to predict a low gravity variation in the stainless steel electron beam welds. As predicted in Equation (B.2), spiking frequency varies inversely with gravity level. Using the experimental conditions, physical properties and beam parameters for the M551 stainless steel experiment and assuming 1120°C of superheat in the melt, Equation (B.2) predicts oscillation frequencies of 22 Hz and 28 Hz for gravity levels of 9.8 m/sec^2 and 9.8 x 10^{-4} m/sec^2, respectively. At a disk rotation rate of 1.58 x 10^{-2} m/sec at the beam impingement point, the spikes would be located 0.72 mm apart and 0.56 mm apart in gravity levels of 9.8 m/sec^2 and 9.8 10^{-4} m/sec^2, respectively. This gravity effect is rapidly dissipated at higher superheats, however, as at 1270°C the spiking frequencies are 41 Hz and 44 Hz at 9.8 m/sec^2 and 9.8 10^{-4} m/sec^2, respectively. This expected gravity-related variation in spiking will be very difficult to observe because it is very difficult to section radial welds precisely along their centerline and even more difficult to etch, polish and perform metallographic analyses on curved sections. No evidence of this possible variation has been reported to date in any of the Phase C investigations being conducted by other contractors or NASA.

REFERENCES

B.1. Laudise, R. A., Carruthers, J. R., and Jackson, K. A.: Crystal Growth, in Annual Review of Materials Science, Vol. 1, 1971, pp. 253-256.

B.2. Laudise, R. A.: The Growth of Single Crystals, Prentice-Hall, Englewood Cliffs, N. J., 1970, pp. 86-103.

B.3. Goldak, J. A., Burbidge, G., and Bibby, M. J.: Predicting Microstructure from Heat Flow Calculations in Electron Beam Welded Eutectoid Steels, Can. Met. Quart., Vol. 9, 1970, p. 459.

B.4. Ibid, p. 467.

B.5. Churchill, S. W., and Hellums, J. D., Dimensional Analysis and Natural Convection, Chem. Engr. Prog. Symp. Ser., Vol. 57, 1964, p. 75.

B.6. Ostrach, S.: Role of Analysis in the Solution of Complex Problems, Third Intl. Heat Trans. Conf., Chicago, August 1966.

B.7. Woods, R. A., and Milner, D. R.: Motion in the Weld Pool in Arc Welding, Welding J., April 1971, p. 163s.

B.8. Kotecki, D. J., Cheever, D. L., and Howden, D. G.: Mechanism of Ripple Formation During Weld Solidification, Welding J., August 1972, p. 386s.

B.9. Brimacombe, J. K., and Weinberg, F.: Surface Movements of Liquid Copper and Tin, Met. Trans., Vol. 3, 1972, p. 2298.

B.10. Wells, O. C., and Everhardt, T. E.: A Note on the Physical Principles Underlying the Formation of the Cavity in Electron Beam Welding, Proc. 4th Symp. Elec. Beam Tech., Boston, 1962, p. 106.

B.11. Grodzka, P. G.: Types of Natural Convection in Space Manufacturing Processes, LMSC-HREC TR D306350, Lockheed Missiles & Space Company, Huntsville, Ala., December 1972.

B.12. Torza, S., Cox, R. G., and Mason, S. G.: Electrohydrodynamic Deformation and Burst of Liquid Drops, Phil. Trans. Roy. Soc. London, Ser. A, Vol. 269, 1971, p. 295.

B.13. Berghmans, J.: Theoretical Investigation of the Interfacial Stability of Inviscid Fluids in Motion, Considering Surface Tension, J. Fluid Mech., Vol. 54, 1972, pp. 129-141.

B.14. Weber, C. M., Funk, E. R., and McMaster, R. C.: Penetration Mechanism of Partial Penetration Electron Beam Welding, Welding J., February 1972, pp. 90s-94s.

B.15. Tong, H., and Geidt, W. H.: A Dynamic Interpretation of Electron Beam Welding, Welding J., June 1970, pp. 259s-266s.

APPENDIX C

DETAILED ANALYSES FOR THE M552 EXPERIMENT

This appendix contains detailed results of theoretical calculations for the M552 experiment. The first portion of the appendix addresses the capillary flow analysis, while the second segment discusses bubble dynamics associated with M552. The last two sections discuss variable gap flow effects and gap size effects on solidification theory, respectively.

C.1 M552 CAPILLARY FLOW

The effect of gap width and low gravity on capillary flow in the M552 Exothermic Brazing Experiment has been studied. Time-to-spread, flow velocities and Reynolds number have been calculated for the configuration shown in Figure C-1. The results are shown in Tables C-1, C-2 and C-3.

The results indicate that:

- Spreading time will be up to 50% shorter in gravity fields anticipated for Skylab than in ground tests.
- Turbulent or oscillatory laminar flow will occur in Skylab processing in certain gaps where only laminar flow could occur in ground tests.

The flow equation for an annulus is given by,

$$u = \frac{\rho g R^2 \phi}{8 \mu h} (h_o - h) \tag{C.1}$$

where

u = velocity

h = axial position in annulus

ρ = density

R = sleeve radius

μ = viscosity

k = tube radius/sleeve radius

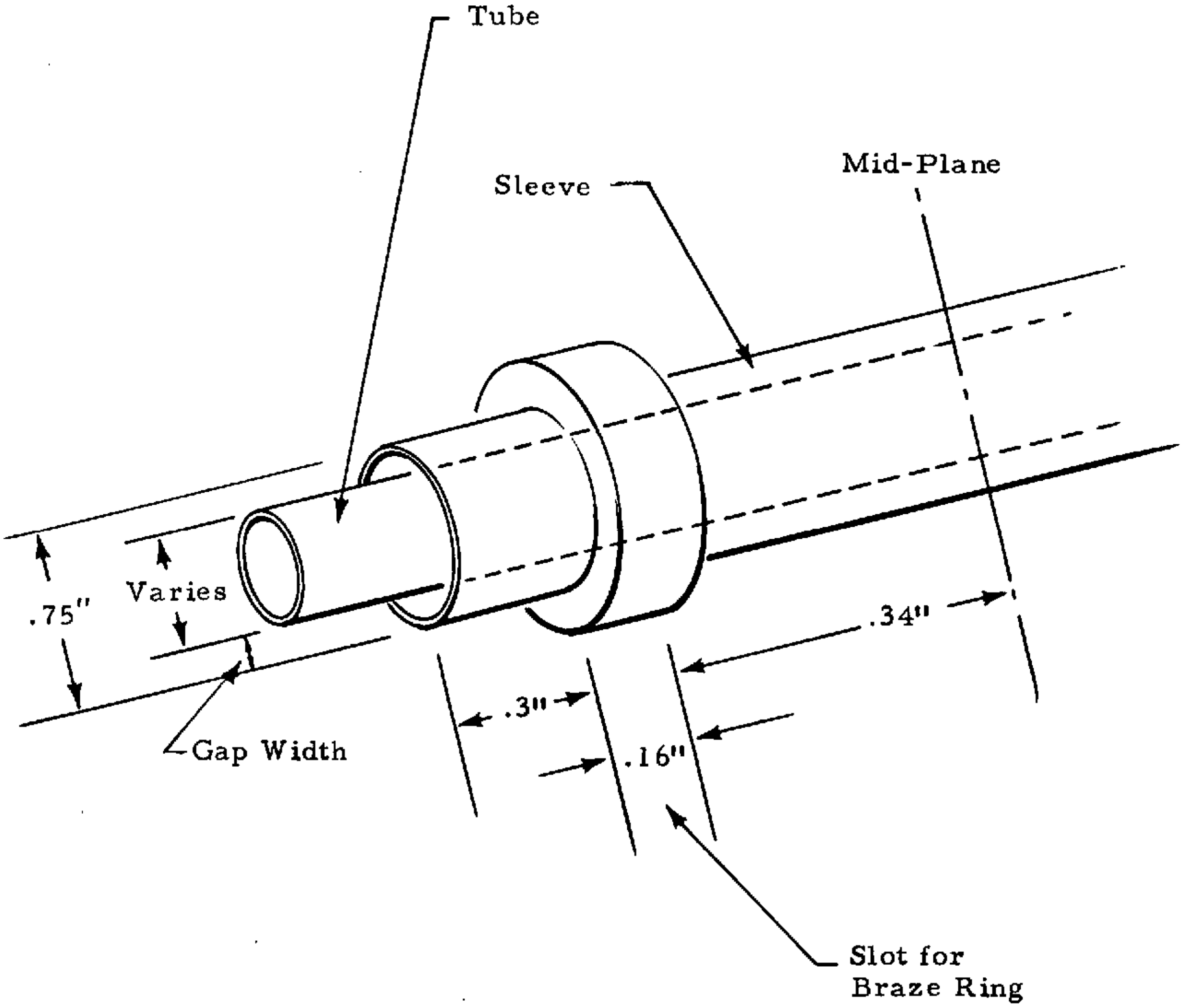

FIGURE C-1. M552 CONFIGURATION

Table C-1
M552 SPREADING TIMES

Gravity (g/g_E)	Gap Width (in.)	Spread Time (Annulus) (μ sec)
$2 \cdot 10^{-6}$	.005 .010 .020 .030*	12.00 6.00 2.97 1.76
1	.005 .010 .020 .030*	13.60 7.47 4.42 3.60

*Assuming no variation in gap width.

Table C-2
M552 FLOW VELOCITIES

Geometry	Gravity (g/g_E)	Gap (in.)	Velocity (u) (cm/sec)
Annulus	$2 \cdot 10^{-6}$	.005 .010 .020 .030*	34 67 134 200
	1	.005 .010 .020 .030*	30 55 90 97
Slot	$2 \cdot 10^{-6}$	.005 .010 .020 .030*	33 66 132 198
	1	.005 .010 .020 .030*	30 53 81 84

*Assuming no variation in gap width.

Table C-3

M552 REYNOLDS NUMBERS

Geometry	Gravity (g/g_E)	Gap (in.)	Re_1	Flow Regime
Annulus	$2 \cdot 10^{-6}$	.005	202	Laminar
		.010	794	Oscillatory
		.020	3200	Turbulent
		.030*	7210	Turbulent
	1	.005	182	Laminar
		.010	650	Laminar
		.020	2170	Oscillatory
		.030*	3490	Turbulent
Slot	$2 \cdot 10^{-6}$	.005	99	Laminar
		.010	395	Laminar
		.020	1580	Laminar
		.030*	3550	Turbulent
	1	.005	90	Laminar
		.010	315	Laminar
		.020	970	Laminar
		.030*	1500	Laminar

*Assuming no variation in gap width.

$$\phi = \frac{1 - k^4}{1 - k^2} + \frac{1 - k^2}{\ell n k}$$

g = gravity

$$h_o = \frac{2\sigma \cos\theta}{\rho \cdot g R (1 - k)}$$

σ = surface tension

θ = contact angle

Equation (C.1) was developed assuming laminar, steady state, incompressible, isothermal flow with $\vec{g}$ opposing the flow direction. It should be a valid approximation for the M552 configuration and processing conditions.

For very narrow gaps, Equation (C.1) reduces to that for flow in a slot which is given by

$$u = \frac{\rho g D^2}{12 \mu h} (h_o - h) \tag{C.2}$$

where

D = slot width

This equation was developed for assumptions similar to those of Equation (C.1) and will be just as rigorous except for geometrical effects.

The spreading time, t, for flow in an annulus can be given by

$$t = \frac{-8\mu}{\rho g R^2 \phi} (h_o \ell n (1 - h/h_o) + h) \tag{C.3}$$

Again, this equation is valid for isothermal, laminar, incompressible flow with $\vec{g}$ opposing flow. Levich [C.1] states it will only be an approximation if $t < \frac{\rho R^2}{\mu}$.

The Reynolds number for flow in an annulus is given as Reference C.2,

$$Re_1 = \frac{2R (1-k) u\rho}{\mu} \tag{C.4}$$

or by Reference C.3,

$$Re_2 = \frac{4R_H u \rho}{\mu} \qquad (C.5)$$

where R_H = hydraulic radius.

The transition from laminar to turbulent flow occurs at $Re_2 \gtrsim 2300$. The transition from laminar viscous flow to oscillatory flow is given by $Re_2 = 700$. By making the transformation, $k = 1 - \epsilon$, and allowing $\epsilon \rightarrow 0$, it can be shown that $Re_1 \rightarrow Re_2$ as $k \rightarrow 1$. Thus the transition points for Re_1 are approximately 700 and 2300 also. The Reynolds number for flow in a slot is defined as

$$Re_s = \frac{\rho u D}{\mu}$$

and the laminar-turbulent transition is at $Re_s \gtrsim 2000$.

C.2 M552 BUBBLE DYNAMICS

Many ground and KC-135 aircraft tests for M552 have exhibited a bubble or void space within the braze structure. Analysis of the movement of such a bubble in low gravity and the nonisothermal conditions of M552 has been initiated. These analyses are applicable to motion of gas bubbles only and will not predict the location of shrinkage voids.

Neglecting wall effects, the limiting velocity of a single bubble moving in a homogeneous liquid under the combined influence of a gravity field and a temperature gradient is given by Reference C.4,

$$u = \frac{2}{3 \mu_g B} \left[3 \mu_g aA \frac{d\sigma}{dT} \frac{dT}{dz} - (\rho_g - \rho_\ell) ga^2 (\mu_g + \mu_\ell) \right]$$

where

$A = 2 + k_\ell / k_g$

$B = 3 \mu_g + 2 \mu_\ell$

k = thermal conductivity

μ = viscosity

a = bubble radius

σ = surface tension

T = temperature
ρ = density
g = gravity

and subscripts ℓ and g refer to the liquid and gas phases, respectively. The temperature gradient affects bubble motion through tangential stresses at the bubble-liquid interface. These stresses are caused by surface tension gradients across the bubble. The surface tension mechanism is termed the Marangoni effect, which can be caused by either temperature or concentration gradients.

The ratio of buoyant/Marangoni forces on the bubble is given by,

$$\gamma = \frac{(\rho_\ell - \rho_g)\, g a\, (\mu_g + \mu_\ell)\, A}{3\, \mu_g \frac{d\sigma}{dT} \frac{dT}{dz}}$$

where γ = buoyancy/surface tension forces. Values of γ for various size bubbles and gravity levels are given below for M552 conditions using a 10°C/cm temperature gradient,

Bubble Diameter (cm)	Gravity (g/g_E)	γ
10^{-4}	1	10^{6}
10^{-4}	10^{-6}	1
10^{-2}	1	10^{5}
10^{-2}	10^{-6}	10^{-1}

Thus, Marangoni forces will be important in Skylab, but not on ground tests.

C.3 CAPILLARY PUMPING IN TAPERED GAPS

Upon melting the braze alloy in the M552 tapered gap specimens (SLN-4, MCN-4, MCN-5 and MCN-6) will have the configuration shown in Figure C-2. Ignoring gravity effects and contact angle hysteresis [C.5 and C.6], the pressure gradients determining flow direction are determined solely by simple capillary effects, as follows [C.7, C.8 and C.9]:

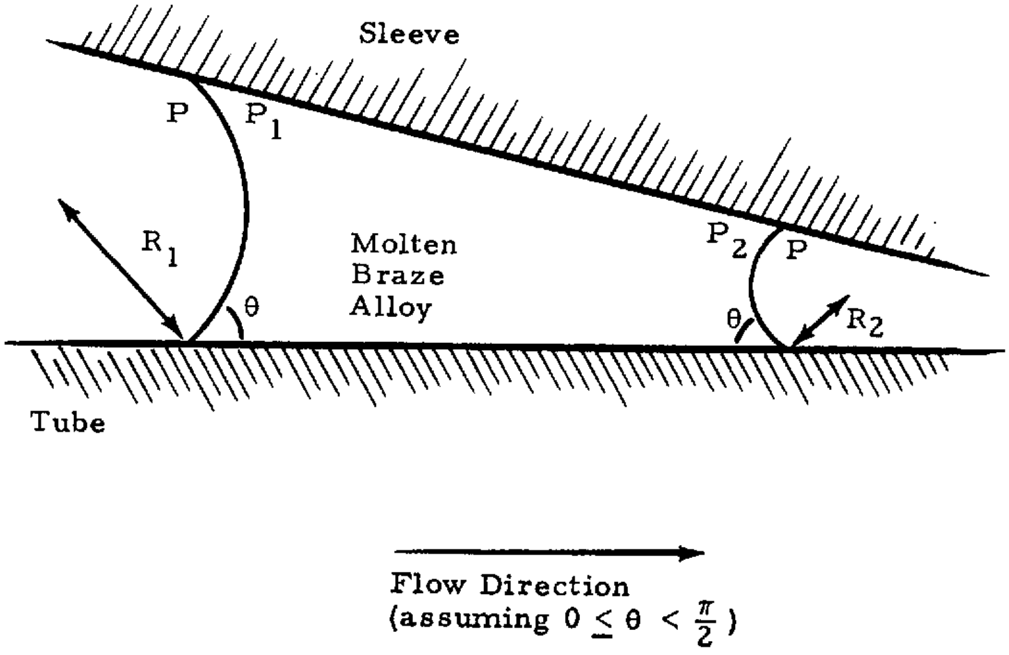

FIGURE C-2. TAPERED GAP CAPILLARY PUMPING FOR THE M552 EXPERIMENT

$$P - P_1 = \frac{2\sigma \cos\theta}{R_1}$$

$$P - P_2 = \frac{2\sigma \cos\theta}{R_2}$$

where the contact angle θ, the pressures P, P_1 and P_2 and the radii of curvature R_1 and R_2 are as shown in Figure C-2. The term σ is the surface tension of the liquid vapor interface.

By eliminating the common term P from these equations, the following results

$$P_1 - P_2 = 2\sigma \cos\theta \left(\frac{1}{R_2} - \frac{1}{R_1} \right) > 0$$

because R_1 is greater than R_2. Thus the molten braze will always flow toward the narrow end of the tube.

The same should be true when gravity is considered because ground tests were conducted vertically and g-levels aboard Skylab II were less than 10^{-6} g_E; i.e., the ratio of hydrostatic to capillary pressures are:

$$\frac{|\rho g h|}{\left| 2\sigma \cos\theta \left(\frac{1}{R_2} - \frac{1}{R_1} \right) \right|} \leq 3 \times 10^{-5}$$

Like gravity effects, contact angle hysteresis (advancing and receding angles differ) should also have negligible effects on final melt position, because hysteresis will only affect the rate of flow and not the flow direction.

C.4 BRAZE SOLIDIFICATION THEORY

In a recent Russian study [C.10], Ryumshim evaluates the influence of the parent metal in determining grain orientation in the braze. It consists of a theoretical consideration of surface (liquid, vapor and solid) energy conditions within narrow braze gaps and experimental findings for Cu-Ni and Ag-Cu systems. These particular alloy systems are pertinent to the materials utilized in the M552 experiment. The primary conclusion is that parent metal influences determine the orientation, nucleation and growth of the braze metal in narrow gaps (less than 0.3 mm), whereas bulk crystallization within the brazing metal predominates with increasing gap size. M552 gap sizes range from 0.13 mm (0.05 inches) to 0.76 mm (0.03 inches).

For highly wetting systems, Ryumshin's theoretical surface energy analysis indicates that the solid substrate will exert its maximum influence on crystallization behavior. Extremely good wetting of the parent metal is always a prerequisite for a brazing metal, thus the preceding condition should always be satisfied in brazing. This condition is surely met in the M552 experiment. In addition, brazing invariably involves parent metal diffusion and dissolution. A contact layer thus forms on the parent metal surfaces with a composition corresponding to the solidus on the brazing-parent metal equilibrium diagram because the supply of diffusing parent metal is infinitely large compared to that of the brazing metal. This layer should have a crystal structure similar to that of the parent metal and promote the growth of oriented crystals in the brazing metal. This orientating influence will be most potent when a continuous series of solid solutions form so that intermediate compounds cannot build up an interlayer which would disrupt the epitaxy.

Ryumshin further states that if brazing and parent metals form secondary phases, the parent metal exerts a much less powerful orienting finluence on braze crystallization, but significant joint structure affects are still possible. Experiments in narrow joints (less than 0.3 mm) with secondary phase crystallization showed that the secondary phase always precipitated on the parent metal and grew directionally normal for the parent metal interface, while in larger gaps bulk crystallization within the braze predominates.

Thus nickel-rich secondary phases nucleating and growing from the sleeve and tube should be more predominant in M552 samples SLN-2, MCN-1 MCN-2 and MCN-3 than in samples SLN-4, MCN-4, MCN-5 and MCN-6. Also the grain orientation within the braze should be similar to that in the stainless steel tube and sleeves in M552 samples SLS-1, SLS-2, MCS-1, -2, -3, -4, -5 and -6.

REFERENCES

C.1. Levich, V.G.: Physicochemical Hydrodynamics, Prentice-Hall, Englewood Cliffs, N.J., 1962.

C.2. Bird, R.B., Stewart, W.E., and Lightfoot, E.N.: Transport Phenomena, Wiley, New York, 1960, p.54.

C.3. Prengle, R.S., and Rothfus, R.R.: Ind. Eng. Chem., Vol. 47, 1955, p. 379.

C.4. Young, N.O., Goldstein, J.S., and Block, M.J.: The Motion of Bubbles in a Vertical Temperature Gradient, J. Fluid Mech., Vol. 6, 1959, p. 356.

C.5. Blake, T.D., and Haynes, J.M.: Contract Angle Hysteresis, Progress in Surface and Membrane Science, Vol. 6, p. 131, 1973.

C.6. Rose, W., and Heins, R.W.: Moving Interfaces and Contact Angle Rate Dependency, J. Colloid Sci., Vol. 17, 1962, pp. 39-48.

C.7. Bikerman, J.J.: Surface Chemistry, Academic Press, New York, 1958, p. 360.

C.8. Petrash, D.A., and Otto, E.W.: Controlling the Liquid-Vapor Interface Under Weightlessness, Astronautics and Aeronautics, Vol. 2, No. 3, March 1964, pp. 56-61.

C.9. Schwartz, A.M.: Capillarity, Ind. Eng. Chem., Vol. 61, No. 1, 1969, pp. 10-21.

C.10. Ryumshin, V.M.: Surface Phenomena in the Crystallization of Brazing Metal, Welding Production, Vol. 17, No. 1, 1970, pp. 12-14.

APPENDIX D

DETAILED ANALYSES FOR THE M553 EXPERIMENT

This appendix contains detailed results of theoretical calculations for the M553 experiment. The first section of this appendix contains analyses of the driving forces, magnitude and pattern of natural convective fluid flows which occur in the Sphere Forming Experiment. Following sections address simple thermal analyses; vaporization; molten pool splattering due to the impinging electron beam; and shrinkage pressure in freezing spheres.

D.1 CONVECTION ANALYSIS

As in the other M512 experiments, the fluid dynamics of the M553 experiment is an important factor in determining the quality of the final product. Flow patterns in the molten material are important because all of the sample materials have low entropies of fusion [D.1]. Thus, their solidification (microstructure) is controlled by the rate of heat transfer removal [D.2], which changes with the fluid flow [D.3 and D.4]. The degree of flow will also determine the amount of mixing attained. If no or little flow were present, all heavier components would segregate to the lower portion of the spheres on earth, but to a negligible extent in the microgravity environment of space. Fluid flow can also affect the shape and release of the specimen while it is retained on the ceramic holder.

Application of dimensional analysis [D.5 and D.6] to the governing equations for eb melting, coupled with ground-based and KC-135 experiments, should enable prediction of the extent of reduction or increase of motion in the molten metal and/or the change in flow pattern in electron beam melting in space. Possible physical forces which could induce fluid flow in the M553 experiment, and their causes, include:

- Effective Gravity Force: Resultant force on weld specimen due to earth's gravity and centrifugal and coriolis forces of orbiting spacecraft.
- Lorentz Force: Electromagnetic forces induced by passage of the electron beam current through the specimen.
- Electrostriction: Stresses induced when electrical permittivity changes with density.

- Magnetostriction: Stresses induced when permeability changes with density
- Electrostatic Force: Caused by presence of excess electrical charge (due to beam current and/or thermionic emission).
- Surface Tension: Tangential stresses at vapor-liquid interfaces can be induced if surface tension depends on temperature and/or concentration. Surface tension will also cause pressure gradients across curved interfaces.
- Density Differences Accompanying Phase Changes
- Beam Force: Impinging electrons giving up their momentum.
- Thermal Expansion: Dilation and compression of fluids whose density changes appreciably with temperature can induce fluid flow.
- Vibration: Uncontrolled movement due to engine operation, astronaut motion, particle impacts, etc.
- Centrifugal and Coriolis: Generated by disk rotation.
- Vapor Pressure: Evaporating molecules impart momentum which leads to normal stresses at vapor-liquid interface.
- Inertia Forces: Tend to sustain induced motions.
- Viscous Forces: Tend to resist driving forces.

Governing Equations

The preceding forces, which could influence fluid flow and solidification, appear explicitly in the following conservation equations which apply to formation of a molten pool by electron beam heating.

Continuity (Mass Balance):

$$\frac{\partial \rho}{\partial t} + \nabla \cdot (\rho \vec{V}) = 0$$

where

ρ = density
$\vec{V}$ = velocity vector
t = time
∇ = "grad" or "del" operator

Momentum:

$$\underbrace{\rho \frac{\partial \vec{V}}{\partial t} + \rho(\vec{V} \cdot \nabla)\, \vec{V}}_{\substack{\text{Inertia}\\ \text{Force}}} = -\nabla P + \underbrace{\mu\, \nabla^2 \vec{V}}_{\substack{\text{Viscous}\\ \text{Force}}} + \underbrace{\rho\, \vec{g}}_{\substack{\text{Gravity}\\ \text{Force}}}$$

$$+ \underbrace{\vec{J} \times \vec{B}}_{\substack{\text{Lorentz and Electro-}\\ \text{magnetostriction}\\ \text{Forces}}} \qquad + \underbrace{\rho_e\, \vec{E}}_{\substack{\text{Electrostatic}\\ \text{Force}}}$$

where

P = pressure
μ = viscosity
$\vec{g}$ = gravity vector
$\vec{J}$ = electrical current density
$\vec{B}$ = magnetic flux density
ρ_e = excess charge density
$\vec{E}$ = electric field density

Energy:

$$\rho C_V \frac{\partial T}{\partial t} + \rho C_V (\vec{V} \cdot \nabla) T = k \nabla^2 T + \Phi + \rho Q$$

$$+ J^2_{c/\sigma'} - (\beta T/K) \nabla \cdot \vec{V}$$

Thermal Expansion
Source

where

T = temperature
C_V = heat capacity
k = thermal conductivity
Φ = viscous dissipation function
Q = internal heat sources
J_c = "conduction" current = $\sigma(\vec{E} + \vec{V} \times \vec{B})$
σ' = electrical conductivity
$\beta = -\frac{1}{\rho} \left(\frac{\partial \rho}{\partial T}\right)_P$
$K = \frac{1}{\rho} \left(\frac{\partial \rho}{\partial P}\right)_T$

Maxwell's Equations:

$$\nabla \times \vec{E} = -\partial \overline{B}/\partial t$$
$$\nabla \times \vec{H} = \overline{J} + \partial \overline{D}/\partial t$$
$$\nabla \cdot \vec{B} = 0$$
$$\nabla \cdot \vec{D} = \rho_e$$

where

$\vec{D}$ = displacement current
$\vec{H}$ = Magnetic flux

Constitutive Relations:

$$\vec{D} = \epsilon' \vec{E}$$
$$\vec{B} = \mu' \vec{H}$$
$$\vec{J} = \sigma'(\vec{E} + \vec{V} \times \vec{B}) + \rho_e \vec{V}$$
$$\rho = \rho_o \left[1 - \beta \Delta T + K \Delta P\right]$$

where

ϵ' = permittivity (dielectric constant)
μ' = permeability

Vapor-Liquid Boundary Conditions:

Force Balance,

$$\overbrace{\left[P^{(2)} - P^{(1)}\right]}^{\text{Beam and Vapor Pressure Forces}} n_i + \underbrace{\frac{\partial \sigma}{\partial X_i} + \sigma \left[\frac{1}{R_1} + \frac{1}{R_2}\right]}_{\text{Surface Tension Forces}} n_i$$

$$= \left[\mu^{(2)} \left(\frac{\partial v_i^{(2)}}{\partial X_k} + \frac{\partial v_k^{(2)}}{\partial X_i}\right) - \mu^{(1)} \left(\frac{\partial v_i^{(1)}}{\partial X_k} + \frac{\partial v_k^{(1)}}{\partial X_i}\right)\right] n_k$$

where $P^{(1,2)}$, $\mu^{(1,2)}$, $v_i^{(1,2)}$, $v_k^{(1,2)}$ are, respectively, the pressures, viscosities, and velocity components in Phases 1 and 2, σ is the surface tension, R_1 and R_2 are the principal radii of curvature of the surface, n_i $(i=1, 2, 3)$ are the components of the unit vector normal to the surface and directed into the interior of Phase 1, and summation over a repeated index $(k=1, 2, 3)$ is assumed.

Energy Balance,

$$\epsilon\sigma \left(T_s^4 - T_\infty^4\right) - k \vec{n} \cdot \nabla T_s = Q_{EB}$$

where

ϵ = emissivity

σ = Boltzmann's constant

T_s = surface temperature

T_∞ = environment temperature

$\vec{n}$ = outward unit normal vector to free surface

Q_{EB} = heat flux from electron beam

Continuity of Velocity,

$$\vec{n} \times (\vec{V}^{(1)} - \vec{V}^{(2)}) = 0$$

$$\vec{n} \cdot \vec{V}^{(1)} = \vec{n} \cdot \vec{V}^{(2)} = 0$$

Solid-Liquid Boundary Conditions:

Along stationary interfaces the no-slip condition (all components of velocity vanish) holds; whereas at moving interfaces (along melting or freezing fronts), a one-dimensional material balance yields

$$u_i = (1 - \rho_s/\rho_L)\, d\delta/dt$$

where

u_i = fluid velocity normal to the interface

δ = position of the interface relative to the origin of the spatial coordinate system

ρ_s = solid density

ρ_L = liquid density

This is the source of the density-difference-accompanying-phase-change force for fluid flow. Also for a melting interface, an energy balance yields:

$$-k\nabla\,(T_L - T_S) = \rho_s\, \lambda\, \frac{d\delta}{dt}$$

where

T_L = liquid temperature at the interface

T_S = solid temperature at the interface

λ = heat of fusion

and

$$T_S = T_M$$

The preceding equations are based on the following assumptions:

- No influence of external fields on physical properties
- No coupling between constitutive flux relations (e.g., no Soret effect)
- Single-component, Newtonian fluid
- Constant physical properties
- Bulk coefficient of viscosity vanishes.

They are written in general vector form wherever possible, since they also apply directly to M551. It should be noted that only the differences in physical properties and geometry will differ in a dimensional analysis of M551 versus M553.

Dimensional Analysis

The controlling physical forces can be determined by non-dimensioning each of the preceding equations and performing an order-of-magnitude comparison on the various dimensionless groups which result [D.5 and D.6]. The key to successful analysis is in choosing the proper reference values; i.e., since no freestream velocity exists, which forces do we equate to estimate a "characteristic" or "typical" velocity. Choosing the proper characteristic velocity is very important, since the reference time, temperature, etc. usually depend on this velocity.

Previous examinations of film showing both KC-135 flight experiments and ground tests for the M553 experiment indicated fluid velocities exceeded 300 cm/sec (p. B-5 of Reference D.7). Continued M553 film analysis has since shown that flow velocities for nickel specimens on both KC-135 and ground tests have been approximately 20 cm/sec. Of the 14 possible forces affecting electron beam melting only those shown in Table D-1 yield characteristic velocities of this order of magnitude. These driving forces consist of couplings involving surface tension, gravity of Lorentz (electromagnetic) forces with inertia forces. Previous studies based on faster velocities had indicated coupling with viscous, rather than inertia, forces as controlling [D.7]. This indicates the importance of choosing the correct characteristic velocity. Preliminary analysis also suggests that magnetostriction forces may also be important, but gross uncertainty in electromagnetic property data for liquid metals precludes any decision at the present time.

The dimensionless momentum equation which determines fluid flow in electron beam melting becomes (upon choosing the surface tension-inertia characteristic velocity),

$$\frac{1}{N_{St}} \rho \frac{\partial \overline{V}}{\partial t} + \frac{1}{N_{Oh}} \rho (\overline{V} \cdot \nabla) \overline{V} = - \frac{1}{2N_{Oh}} \nabla P + \nabla^2 \overline{V} + \frac{N_{Bo}}{N_{Oh}} (\rho \overline{g}) + \frac{2N_{MI}}{N_{Oh}} (\overline{V} \times \overline{B}) \times B \qquad (D.1)$$

where

N_{St} = Stokes number = $\mu t_o / \rho_o L$

= duration of process/residence time

N_{Oh} = Ohnesorge number = $\mu / \sqrt{\rho_o L S T_o}$

= viscous force/surface tension force

N_{Bo} = Bond number = $\rho_o g_o L^2 / ST_o$

= gravity force/surface tension

N_{MI} = Magnetic interaction number = $\dfrac{B_o^2 L}{2\mu'_o ST_o}$

= magnetic force/surface tension

Using physical property data for nickel and beam parameters for the M553 experiment, the equation reduces to

Table D-1

PROBABLE CHARACTERISTIC VELOCITIES IN ELECTRON BEAM MELTING

Controlling Forces	Velocity	
	Functional Form	Value (cm/sec) for Nickel in M553
Inertia = Surface Tension	$(ST/\rho L)^{1/2}$	20
Inertia = Lorentz	$(\sigma' E^2 L/\rho)^{1/3}$	1
Inertia = Gravity	$(gL)^{1/2}$	18 at 1 g_E 6 at $10^{-4} g_E$
Viscous = Lorentz	$(\sigma' E^2 L^2/\mu)^{1/2}$	7

$$10^3 \rho \frac{\partial \overline{V}}{\partial t} + 10^3 \rho (\overline{V} \cdot \nabla) \overline{V} = -10^3 \nabla P + \nabla^2 \overline{V}$$

$$+ G(\rho \overline{g}) + 10^{-1} (\nabla \times \overline{B}) \times \overline{B}$$

where

$G = 10^3$ for earth gravity

$G = 10^{-1}$ for expected Skylab gravity.

This order-of-magnitude analysis indicates that surface tension driven convection will occur both in ground tests and for Skylab conditions because $N_{Oh} << 1$. This is confirmed by KC-135 M553 tests. Furthermore, gravity driven convection will exist on ground tests, but will be negligible in the reduced gravity of Skylab. Thus different forces will control convection on earth versus Skylab. The preceding analysis also indicates that electromagnetic or Lorentz forces will be negligible with regard to causing fluid motion.

The surface tension driving force considered above is actually a surface tension gradient caused by radial and lateral temperature gradients. Ignoring convection, gradients of at least several hundred degrees Celsius per centimeter have been predicted during melting [D.8]. It can be shown by dimensional analysis (equate inertial and viscous terms) that the motion caused by the initial temperature gradients will occur in less than 0.1 second and can persist for 60 seconds after removing the driving force. This means that there will be some fluid motion during solidification if the M553 specimens freeze after 30 to 40 seconds as predicted.

Values of the pertinent dimensionless groups for the remaining M553 materials are given in Table D-2. As can be seen, no significant changes are evident from the preceding conclusions for pure nickel.

It should also be mentioned that the effects on fluid motion of surface free charges (excess electrostatic charge) and related electric and magnetic forces at the drop surfaces have been examined. The results of the examination indicate that these surface charges are negligible driving forces for fluid motion. These results were also reviewed by Professor J. R. Melcher of MIT's Electrical Engineering Department, and he was in full agreement with these results [D. 9]. Furthermore, from the manner in which patches of surface contaminants moved about in the ground films, it is apparent that surface tension driven flows due to concentration gradients are also important in this experiment. No reliable data exist, however, on what these impurities are, nor what the value of surface tension gradient with composition is. Thus the Marangoni effects are limited to thermal differences only in this study.

Table D-2

M553 DIMENSIONAL ANALYSIS

Material	N_{Oh}	N_{Bo}	$\frac{1}{N_{Oh}}$	$\frac{N_{Bo}}{N_{Oh}}$*	$\frac{N_{Bo}}{N_{Oh}}$†
Ni-Sn	4.4×10^{-4}	1.50	2292	3437	.34
Ni-Ag	5.0×10^{-4}	1.53	1991	3043	.30
Ni-Cu	4.45×10^{-4}	1.54	2107	3241	.32

*With Earth gravity (9.8 m/sec^2)

†With 10^{-4} Earth gravity

Flow Patterns

The aforementioned difference in controlling forces between terrestrial and space processing of the M553 experiment should result in altered flow patterns between these two conditions. From a knowledge of flow patterns generated by surface tension versus buoyancy controlled natural convection on Earth, the situation illustrated in Figure D-1 would no doubt exist during melting on Earth, while that shown in Figure D-2 would prevail in space.

The patterns shown in Figure D-2 are based on the fact that surface tension is stronger in cooler regions; therefore the coolest portion of the specimen will exert the strongest "pull" on the surface. The buoyancy modification exhibited in Figure D-1 reflects the rise of warmer portions of fluid in a gravity field coupled with surface tension flows.

D.2 M553 THERMAL ANALYSIS

A critical question which must be answered for the M553 experiment is, "How long will it take for the released specimens to cool down to a "touch" temperature of 40°C?" Two separate models were formulated to study this problem. The results are shown in Table D-3. These results are based on the specimens being at the melting point (no superheat) upon release.

Specimen conditions reported in Table D-3 include: free floating in vacuum; free floating and chamber backfilled with cabin atmosphere of $3.45 \cdot 10^4$ N/m^2 (5 psi) mixture of 70% O_2 and 30% N_2 two minutes after specimen release; and free-floating specimen and the chamber pumped with a steady stream of cabin atmosphere at a flow rate of $2.4 \cdot 10^{-3}$ m^3/sec (5 cu ft/min). In the last case, the flow is considered to start two minutes after specimen release.

Results shown in Table D-3 indicate that the chamber will be safe to open eight minutes after release of the last M553 specimen if a cabin atmosphere flow of 5 cu ft/min is established within the chamber two minutes after release of this last specimen. Otherwise, up to several hours may be needed for specimen cooldown to touch temperature. If the chamber is backfilled with 5 psi cabin atmosphere, cooldown time is roughly 35 to 40 minutes with 5 psi air versus several hours, unless the spheres remain attached to the chamber walls. It is unlikely, however, that all 11 of the release specimens will remain attached to a solid surface.

The first model formulated was for a free-floating sphere being cooled by conduction and convection to an ambient atmosphere and/or

Table D-3

M553 COOLDOWN TIMES

Thermal Condition of Specimen	Cooldown Time*	Chamber Wall Temperature (°C)
Free floating in vacuum	3.3 hr	26.7
	2.6 hr	15.6
	2.5 hr	-273
Sticks to wall	6 sec	26.7
Sticks to wall for 0.5 sec	3.3 hr	26.7
Free floating and chamber backfilled with $3.5 \cdot 10^4$ N/m^2 mixture of 70% O_2 and 30% N_2	34 min	26.7
Free floating and $3.5 \cdot 10^4$ N/m^2 70% O_2 - 30% N_2 cabin air flow at $2.4 \cdot 10^{-3}$ m^3/sec through chamber	7.7 min	26.7

*For individual 0.64 cm molten nickel spheres at their melting point to reach 40°C.

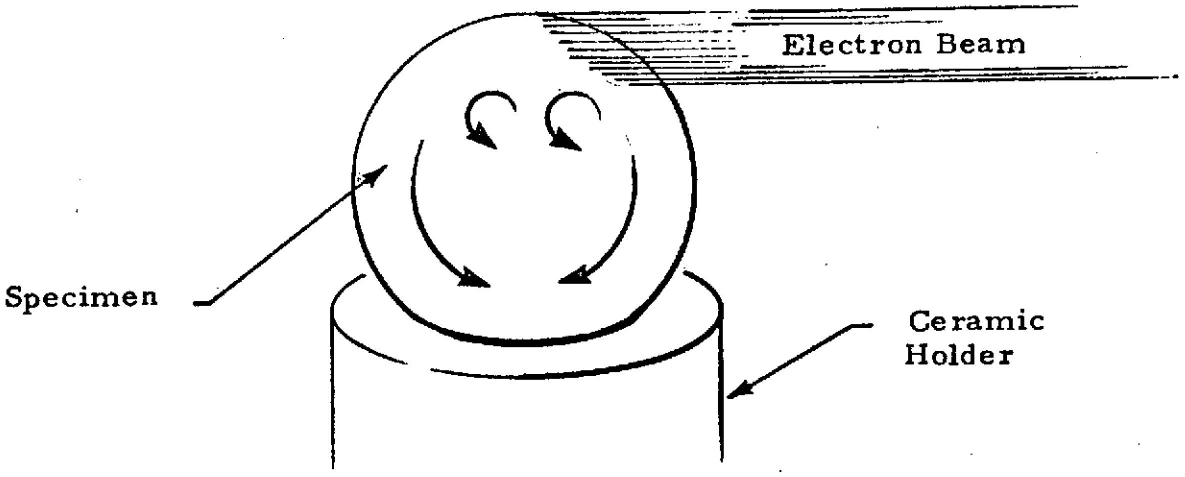

FIGURE D-1. CONVECTIVE PATTERNS IN THE M553 SPECIMEN DURING MELTING ON EARTH

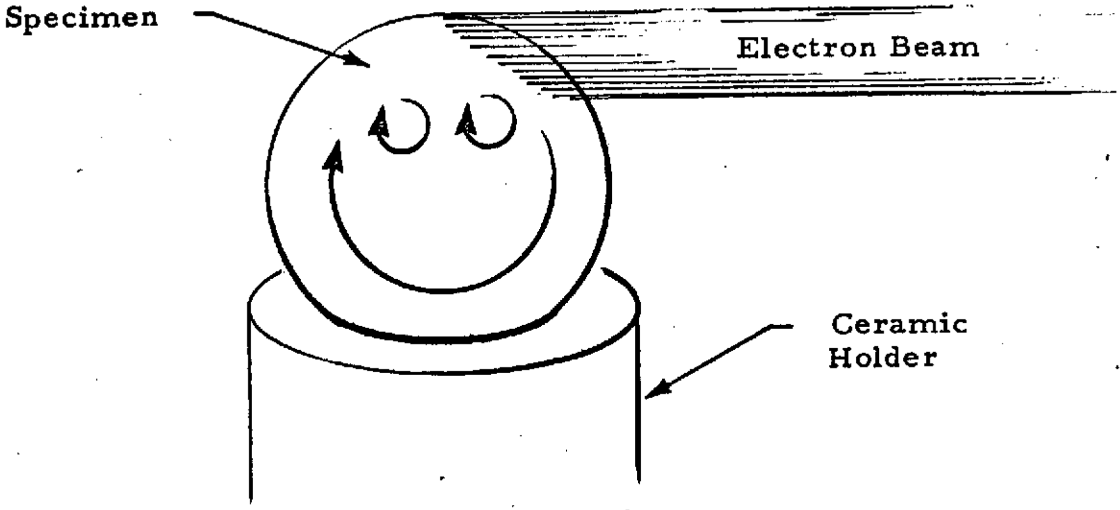

FIGURE D-2. CONVECTIVE PATTERNS IN THE M553 SPECIMEN DURING MELTING IN SPACE being cooled by radiation to the chamber walls. Assuming that only sensible heat is being removed (no phase change) and that thermal diffusivity is infinitely large (an extremely good conductor), the energy balance becomes

$$\rho V C \frac{\partial T}{\partial t} = -A \sigma \epsilon \left(T^4 - T_w^4\right) - A h \left(T - T_o\right) \qquad \text{(D.2)}$$

where

T = sphere temperature

T_w = wall temperature

T_o = chamber atmosphere temperature ($\approx T_w$)

σ = Boltzmann's constant

ϵ = emissivity of sphere

h = convective heat transfer coefficient

A = surface area of specimen

ρ = specimen density

V = volume of specimen

C = heat capacity of specimen

t = time

The coefficient h, for stationary cabin atmosphere, can be estimated by Reference D.10.

$$h = \frac{k}{D} \left(2 + Gr^{1/4}\, Pr^{1/3}\right)$$

where

k = thermal conductivity

D = sphere diameter

Gr = Grashof number

Pr = Prandtl number

For the condition of cabin air through the chamber, the heat transfer coefficient for the sphere (forced convection cooling of small spheres) can be obtained from a plot of Nusselt number versus Reynolds number and Prandtl number given in Reference(D.10).

Equation D.2 is valid for either a molten or solidified specimen. A computer program written in FORTRAN IV was written to solve Equation D.2 utilizing a fourth-order Runge-Kutta numerical algorithm. The output of this program is a temperature versus time profile.

An estimate of the freezing time, t_f, for this model, again assuming infinite thermal diffusivity is given by

$$t_f = \frac{\rho R \lambda}{3\left[\epsilon \sigma T^4 - h (T - T_w)\right]} \qquad \text{(D.3)}$$

A correction time, t_c, for the effect of finite thermal conductivity is given by

$$t_c = \rho C R^2 / k \qquad \text{(D.4)}$$

Thus the time for a molten, free-floating specimen at its melting point to cool down to touch temperature is given by

$$t_T = t_f + t_s + t_c$$

where

t_T = total time to reach touch temperature

t_s = time to remove sensible heat (from Equation D.2)

The second model was developed for a specimen attached to the chamber wall being cooled by conduction to the wall and radiation. The chamber atmosphere was assumed to be a hard vacuum. Again, assuming that only sensible heat is being removed and that the specimen is a perfect conductor, the energy balance becomes,

$$\rho V C \frac{\partial T}{\partial t} = -A' \epsilon \sigma (T^4 - T_w^4) - A_w h_e (T - T_w) \qquad \text{(D.5)}$$

where

A_w = contact area between the specimen and chamber wall

A' = free surface area of specimen

h_e = effective heat transfer coefficient to account for conduction losses

Over the area of contact, A_w, the chamber wall can be assumed to be flat, therefore A_w and A' can be derived using simple geometry and are given by

$$A_w = \frac{\pi^{1/3} \sin^2\theta \, V^{2/3}}{(1 - \cos\theta)^{4/3} \left(\frac{2 + \cos\theta}{3}\right)^{2/3}}$$

$$A' = 2\left(\frac{1 - \cos\theta}{\sin^2\theta}\right) A_w$$

where

θ = contact angle.

The effective transfer coefficient is given by

$$h_e = k_w/L$$

where

k_w = thermal conductivity of chamber wall

L = some characteristic length for conduction in the wall.

The characteristic length L can be estimated by

$$L = Dk_w/2k$$

The freezing time and correction time for finite conductivity can be estimated from Equations (D.3) and (D.4), respectively.

Equation (D.5) can be solved using the algorithm developed for Equation (D.2).

D.3 VAPORIZATION IN M553

A brief study of vaporization losses expected for nickel, aluminum, copper and silver under conditions expected during the melting portion of the M553 experiment indicates that aluminum will evaporate 50 times faster than silver and 10 times faster than copper. Thus, Ni-Aℓ(5%) should not be considered as a material in the sphere forming experiment. The effect of concentration was included and the other sample materials were thus Ni-Ag(1%), Ni-Cu(30%), and pure nickel.

The above data were obtained using Langmuir's formula

$$\dot{m} = P_v \sqrt{\frac{M}{2\pi RT}} \quad \text{kg/m}^2\text{-sec}$$

where

$\dot{m}$ = vaporization rate

M = molecular weight

P_v = partial pressure

T = surface temperature

R = gas constant

Surface temperatures were conservatively estimated to be 1725°K.

D.4 MELT SPLATTERING INSTABILITY

In both the M551 and M553 experiments, the heat released to the metal specimens by the impinging electron beam enables a molten pool to form. A question arises as to the stability of these molten liquids in low gravity. At least one of the KC-135 M553 specimens was seen to break up violently into many smaller liquid spheroids upon complete melting. The electron beam was still hitting the specimen during break up. A similar instability might develop in the molten puddle formed during the dwell mode of the M551 experiment, wherein the liquid might not adhere and separate from the solid disk (violent splattering).

There are at least three different mechanisms which might explain the instability observed in the M553 KC-135 specimens. Upon melting, the specimen may have experienced violent degassing which could have led to droplet breakup. Another mechanism might be electromagnetic forces for the electron beam and the fluid flow field set up in the molten metal by both thermal gradients, Lorentz and other forces. Lastly, the momentum force associated with the impinging electron beam might have set up unstable surface oscillations on the molten metal.

The latter instability mechanism has been treated recently by Berghmans [D.11]. He performed a theoretical study of fluid interface stability with special attention being given to the role of surface tension. A detailed examination of this instability mechanism for both the M551 and M553 experiments is given in Appendix B where it is shown that the electron beam momentum force is not the cause of splattering in either of these experiments.

D.5 SHRINKAGE PRESSURE IN FREEZING SPHERES

When spherical melts solidify, the innermost melt is the last to freeze. The advancing outer solid shell leads to hydrostatic tensions, even negative pressures, in the residual liquid and the general plastic collapse of the spherical casting. The contraction (about 3% for most metals) is caused by solidification shrinkage. Several recent analyses have been performed for this configuration [D. 12 through D. 14], and two extreme cases which could exist are shown in Figures D-3 and D-4. In Figure D-3 the residual liquid is considered to have undergone cavitation. The homogeneous fracture pressure of most liquid metals is thought to be on the order of -10^{-5} atm; however, heterogeneous nucleation may be possible at less negative pressures.

The tensile pressures within the residual liquid can be calculated assuming various growth rates and outer shell deformation modes: elastic-plastic, Bingham, viscous or creep flow. Using the creep flow model, negative pressures in the liquid core of 1 cm radius nickel sphere are shown in Figure D-5 using initial pressure of 1 atm. Nickel spheres in the M553 experiment are 0.32 cm in radius. The tensile pressures will be lesser in wide freezing range alloys [D.14].

Thus the value of possible shrinkage pressure developed within spherical solidifying castings has been evaluated for various materials exhibiting various deformation characteristics. The maximum attainable stresses in aluminum, copper, nickel and iron are in the range -10^4 to -10^{-5} atm. The exact values are uncertain because the solidification rate of a sphere is not accurately known, but it is probable that homogeneous nucleation is not a feasible mechanism for the initiation of porosity in solidifying metals. These extremely low pressures may help explain the unexpected results being found by other M553 contractor investigators.

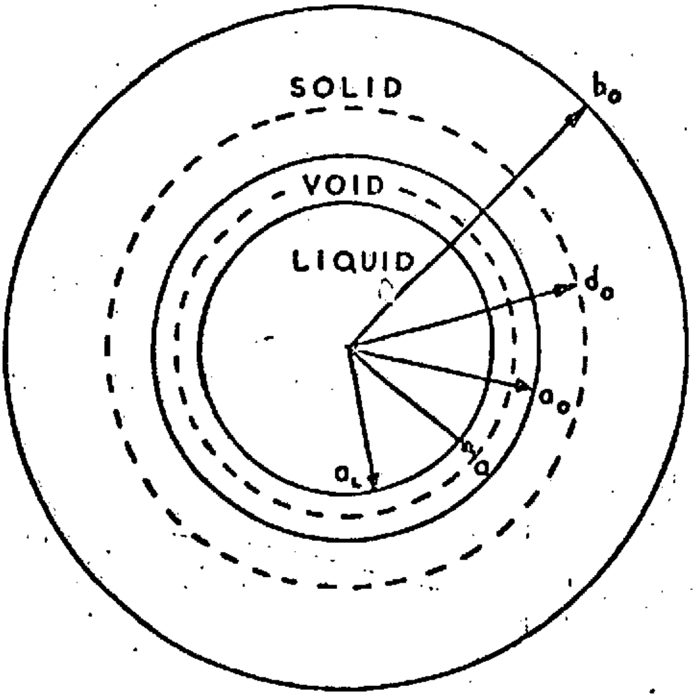

FIGURE D-3. UNSTRAINED OUTER CASTING AND HOMOGENEOUS NUCLEATION OF RESIDUAL LIQUID UNDER EXTREME NEGATIVE PRESSURES [D. 12]

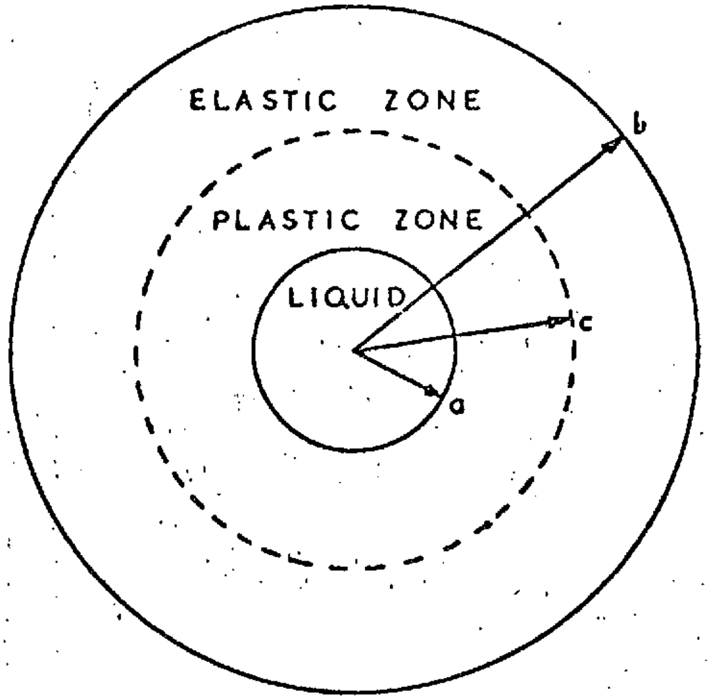

FIGURE D-4. STATE OF A SOLIDIFYING SPHERICAL CASTING WITH EXTERIOR SHELL DEFORMATION [D.12]

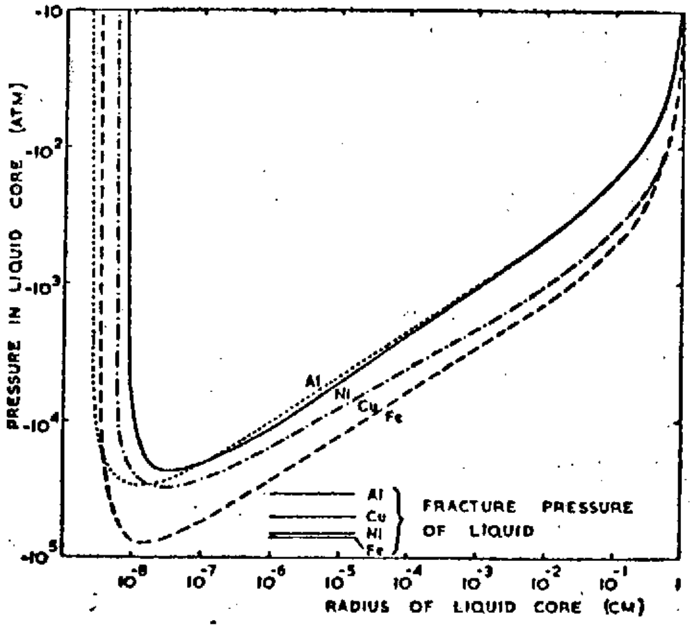

FIGURE D-5. HYDROSTATIC TENSIONS IN THE LIQUID CORE OF 1 cm RADIUS CASTINGS OF ALUMINUM, COPPER, NICKEL, AND IRON CALCULATED FROM THE CREEP MODEL [D.13]

REFERENCES

D.1. Laudise, R. A., Carruthers, J. R., and Jackson, K. A.: Crystal Growth, in Annual Review of Materials Science, Vol. 1, 1971, pp. 253-256.

D.2. Laudise, R. A.: The Growth of Single Crystals, Prentice-Hall, Englewood Cliffs, N. J., 1970, pp. 86-103.

D.3. Goldak, J. A., Burbidge, G., and Bibby, M. J.: Predicting Microstructure from Heat Flow Calculations in Electron Beam Welded Eutectoid Steels, Can. Met. Quart., Vol. 9, 1970, p. 459.

D.4. Cole, G. S.: Transport Processes and Fluid Flow in Solidification, in Solidification, American Society for Metals, Metals Park, Ohio, 1971, pp. 201-274.

D.5. Churchill, S. W., and Hellums, J. D.: Dimensional Analysis and Natural Convection, Chem. Engr. Prog. Symp. Ser., Vol. 57, 1964, p. 75.

D.6. Ostrach, S.: Role of Analysis in the Solution of Complex Problems, Third Intl. Heat Trans. Conf., Chicago, August 1966.

D.7. Lockheed Missiles & Space Company, Convection in Space Processing — Bimonthly Progress Report, LMSC-HREC D306219, 28 September 1972, p. B-9.

D.8. Lockheed Missiles & Space Company, Research Study on Materials Processing in Space Experiment M512 — Monthly Progress Report, LMSC-HREC PR D306549, Huntsville, Ala., 28 March 1973.

D.9. Melcher, J. R.: Discussions on Electrohydrodynamic Applications in Space Processing, Marshall Space Flight Center, Huntsville, Ala., 11 June 1973.

D.10. Bird, R. B., Stewart, W. E., and Lightfoot, E. N.: Transport Phenomena, Wiley, New York, 1960, p. 413.

D.11. Berghmans, J.: Theoretical Investigation of the Interfacial Stability of Inviscid Fluids in Motion, Considering Surface Tension, J. Fluid Mech., Vol. 54, 1972, pp. 129-141.

D.12. Campbell, J.: Shrinkage Pressure in Castings (The Solidification of a Metal Sphere), Trans. Met. Soc., AIME, Vol. 239, 1967, p. 138.

D.13. Campbell, J.: Hydrostatic Tensions in Solidifying Materials, Trans. Met. Soc., AIME, Vol. 242, 1968, p. 264.

D.14. Campbell, J.: Hydrostatic Tensions in Solidifying Alloys, Trans. Met. Soc., AIME, Vol. 242, 1968, p.268.

☆U.S. GOVERMENT PRINTING OFFICE 1974 — 640-447 / 136 REGION NO. 4